aerospace

MDPI

Article

Hypersonic Impact Method for Aerodynamics and Convective Heating (HI-Mach) with Sensitivities †

Jeremiah Goates *, Logan Freeman, Nathan Hoch and Douglas Hunsaker

Mechanical and Aerodspace Engineering, College of Engineering, Utah State University, 4130 Old Main Hill, Logan, UT 84321, USA; logan.freeman@usu.edu (L.F.); doug.hunsaker@usu.edu (D.H.)

* Correspondence: a02267689@usu.edu

† This paper is a compilation of three papers presented at Goates, J.K.; Freeman, L.B.; Hunsaker, D.F. Theory and Implementation of a Rapid Hypersonic Impact Method (HI-Mach) Part I: Aerodynamics. In Proceedings of the AIAA SciTech 2025 Forum, Orlando, FL, USA, 6–10 January 2025; Freeman, L.B.; Goates, J.K.; Hunsaker, D.F. Theory and Implementation of a Rapid Hypersonic Impact Method (HI-Mach) Part II: Convective Heating. In Proceedings of the AIAA SciTech 2025 Forum, Orlando, FL, USA, 6–10 January 2025; Freeman, L.; Goates, J.K.; Hoch, N.H.; Hunsaker, D.F.; Galbraith, M.C. Theory and Implementation of Shape Sensitivities in a Rapid Hypersonic Impact Method (HI-Mach). In Proceedings of the AIAA SCITECH 2026 Forum, Orlando, FL, USA, 12–16 January 2026.

Abstract

The purpose of this paper is to present the development of an engineering level code for calculating hypersonic aerodynamics and convective heating, HI-Mach. Novel to this paper are the use of analytic methods for streamline tracing and the direct differentiation of geometric sensitivities for both forces and heat load. Independent panel inclination methods calculate the pressure distribution on the surface of a hypersonic vehicle. Normal shock relations provide the thermodynamic state on each panel. Streamlines are integrated using closed-form streamline equations. Flat plate formulas corrected for compressibility calculate the skin friction coefficient and acreage heat flux on each panel. Formulas for heating on stagnation points and lines, including effects of ellipticity and sweep, are used to calculate stagnation region heating. A method for obtaining the sensitivities of a quantity of interest with respect to the geometry in a hypersonic panel code is described. These are obtained using direct analytical derivatives. The approach is precise and has been thoroughly tested against finite differencing. HI-Mach provides results orders of magnitude faster than would be obtained by CFD. Results from HI-Mach are analyzed and compared to experimental results for the HL-20 lifting body geometry. For the aerodynamic characteristics, HI-Mach predicted force coefficients within 12% of experimental results at $M\infty = 4.5$ and 21% at $M_\infty = 1.6$. Heating results for the HL-20 match experimental and CFD results to within 20% over a wide range of operating conditions.

Keywords: hypersonics; conceptual design; impact methods; sensitivities

Check for updates

Academic Editor: Sebastian Karl

Received: 12 March 2026
Revised: 10 April 2026
Accepted: 10 April 2026
Published: 15 April 2026

Copyright: © 2026 by the authors. Licensee MDPI, Basel, Switzerland. This article is an open access article distributed under the terms and conditions of the Creative Commons Attribution (CC BY) license.

1. Introduction

The difficulties of the hypersonic flight environment require integrated and optimized designs. A successful hypersonic vehicle must withstand high heat fluxes and extreme aerodynamic loads while maintaining performance. Thermal protection systems, control surfaces, propulsion elements, and other components become increasingly interconnected and integrated at high speeds. Therefore, designing a complete vehicle requires many iterations of redesign and analysis on the entire vehicle.

As a result, there is a need for rapid analysis tools in hypersonic development. The required computational resources and time for high-fidelity CFD tools make them difficult to use in preliminary design phases where the rapid iteration of designs is necessary. Hypersonic impact methods, or local surface inclination methods [1–4], allow for a rapid aerodynamic analysis of arbitrary hypersonic vehicles. Unlike panel methods, which set up and solve linear systems to analyze subsonic and supersonic aircraft [5], impact methods employ property calculations for each panel independently of surrounding panels. More specifically, the pressure coefficient on each panel is solely a function of the freestream properties and the local surface inclination. Atue and Bruce [6] have shown that these reduced-order methods are capable of runtimes near 10^0 s on a laptop. This is compared to STAR-CCM runtimes between 10^2 and 10^4 s using a cluster of 128 processors. These methods, while simple, maintain their value in a world of high-fidelity simulations.

Many codes using hypersonic impact methods for calculating the aerodynamic and heating characteristics of hypersonic vehicles are currently available [7–10]. One of the first of these codes was the Hypersonic Arbitrary Body Program (HABP) developed by Gentry and Smyth at Douglas Aircraft Company in 1964 [9]. HABP provides the user with a large suite of methods to calculate inviscid pressures. In addition, HABP uses an integral boundary layer method to calculate the viscous forces. However, HABP is limited by the lack of heating calculations and need for structured meshes. A second code that is used widely is Configuration-Based Aerodynamics (CBAERO) developed by David Kinney [7]. Unlike HABP, CBAERO allows for the use of unstructured meshes and provides heating calculations. CBAERO uses simpler flat plat coorelations for viscous forces and has a more limited suite of inviscid pressure methods. Table 1 summarizes the features of these two existing tools with the present method, HI-Mach.

Table 1. HI-Mach feature comparison.

	HI-Mach	**CBAERO**	**HABP**
Pressures	Classical	Classical	Large Suite
Streamlines	Unique Formulation	N/A	Runge Kutta
Skin Friction	Flat Plate	Axisymmetric	Integral Boundary Layer
Heating	Convective	Convective and Radiative	None
Sensitivities	Direct Forces and Heating	Forces	None
Mesh	Unstructured	Unstructured	Structured

Hypersonic impact methods are computationally cheap. This makes them an ideal tool for use in optimization processes. Optimization processes seek to improve the performance of an initial design by changing design parameters. For example, optimizing a hypersonic vehicle to reduce peak heat flux would involve making the nose more blunt. Many optimization tools use the gradient of quantities of interest with respect to design parameters to change the design. In Navier–Stokes CFD codes, the gradient can be computed with the adjoint method [11–13]. Hypersonic impact methods do not involve direct solutions to PDEs or solutions of large linear systems; they are therefore amenable to direct differentiation for the computation of the gradients. CBAERO has previously been used for the optimization of hypersonic vehicles through direct differentiation [14]. However, only the inviscid effects were considered in the aforementioned work.

This paper seeks to clearly present the theory of hypersonic impact methods. This paper also presents the implementation of the theory into a useful hypersonic impact tool. The presented tool, a Hypersonic Impact Method for Aerodynamics and Convective Heating (HI-Mach), takes advantage of modern tools such as object oriented programming, parallel programming, and unstructured grids. The rapid nature of HI-Mach allows it to

be used in trajectory optimization and vehicle design [15,16]. This paper also presents the theory and implementation of sensitivity calculations within the framework of HI-Mach. Results of the aerodynamic, heating, and sensitivity solutions are presented. The accuracy of the code is evaluated against experimental aerodynamic and heating data for the HL-20, a NASA-designed lifting reentry body [17], and other canonical geometries.

The main contributions of this paper are as follows. First, this paper provides a unified presentation of hypersonic impact methods and their implementation into a useful tool. Second, this paper uses a novel streamline tracing method that takes advantage of analytical equations for surface streamlines. Lastly, this paper presents direct differentiation methods for geometric sensitivities of aero and thermal properties.

2. Theory

The purpose of HI-Mach is to produce the forces and heat load on a given body. Figure 1 displays the process by which these quantities are obtained. The presentation of these methods is organized as follows. First, the processes for computing the aerodynamic characteristics of a hypersonic body are presented. These include the inviscid aerodynamics calculated using various local inclination methods, the addition of viscous effects through compressible flat-plate correlations, and an analytical streamline-tracing algorithm for efficient calculation of running length. Second, the processes for computing the convective heating to a body in hypersonic flow are described. These include stagnation and acreage heating relations, mesh curvature methods, and wall boundary conditions. Finally, the sensitivities of the preceding calculations to the geometry are derived.

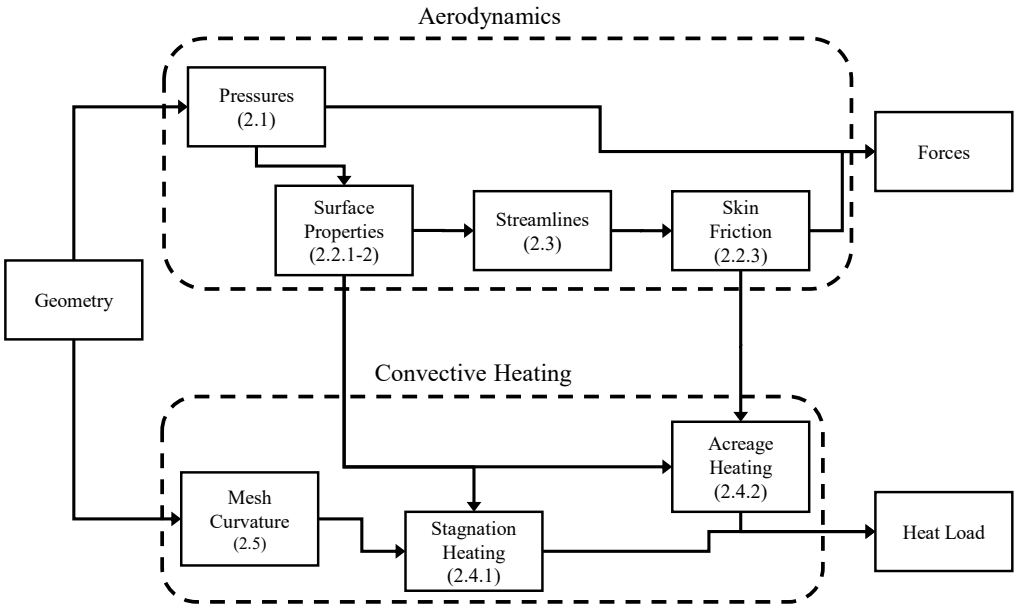


Figure 1. Organizational flow chart for methods within HI-Mach.

2.1. Inviscid Aerodynamics

The inviscid aerodynamic methods in HI-Mach provide the pressure on the surface of the given body. This pressure is used to calculate the forces on the body as well as the other surface properties (Mach number, viscosity, temperature, etc.).

2.1.1. Local Inclination Methods

In this paper, the inviscid aerodynamics of a hypersonic vehicle are calculated using local inclination methods [4]. In all of these methods, the pressure coefficient on each panel is a function of the inclination of the panel to the freestream. This is given by

$$\theta = \cos^{-1}\left(\frac{\hat{\boldsymbol{n}} \cdot \hat{\boldsymbol{V}}_\infty}{|\hat{\boldsymbol{V}}_\infty|}\right) - \frac{\pi}{2} \tag{1}$$

where $\hat{\boldsymbol{n}}$ is the normal vector of the panel and $\hat{\boldsymbol{V}}_\infty$ is the freestream velocity vector. Surfaces where $\theta > 0$ are classified as windward surfaces, and surfaces where $\theta \leq 0$ are classified as leeward surfaces. Different relations are used for calculating the pressure coefficient on the windward and leeward surfaces. Once the pressure coefficient, C_P, is obtained for each panel i, the force coefficient on the body becomes

$$C_F = \frac{1}{A_{\text{ref}}} \sum_{i=1}^{m} C_{P_i} A_i \hat{\boldsymbol{n}}_i \tag{2}$$

where m is the number of panels, A_i is the panel area, and A_{ref} is the reference area for the vehicle. The moment coefficient on the body can be calculated in a similar manner by

$$C_M = \frac{1}{A_{\text{ref}} l_{\text{ref}}} \sum_{i=1}^{m} C_{P_i} A_i (\hat{\boldsymbol{c}}_{\boldsymbol{i}} \times \hat{\boldsymbol{n}}_i) \tag{3}$$

where $\hat{\boldsymbol{c}}_{\boldsymbol{i}}$ is the location of the centroid of the panel relative to the vehicle center of gravity and l_{ref} is the reference length for the vehicle.

2.1.2. Windward Pressure Methods

The first of the windward pressure methods are the straight and modified Newtonian methods. For both of these methods, the pressure coefficient is given by

$$C_{P,\text{Newtonian}} = C_{P_{\max}} \sin^2 \theta \tag{4}$$

where $C_{P_{\max}}$ varies between the two methods. The straight Newtonian method defines $C_{P_{\max}} = 2$ for all cases. The modified Newtonian method introduces Mach number dependence by defining $C_{P_{\max}}$ as the stagnation pressure coefficient aft of a normal shock as suggested by Lees [18]. This results in

$$C_{P_{\max}} = \frac{2}{\gamma M_\infty^2} \left\{ \left[\frac{(\gamma+1)^2 M_\infty^2}{4\gamma M_\infty^2 - 2(\gamma-1)} \right]^{\frac{\gamma}{\gamma-1}} \left[\frac{1 - \gamma + 2\gamma M_\infty^2}{\gamma+1} \right] - 1 \right\} \tag{5}$$

The Newtonian methods only apply to the windward surface of the body. Unless another method for the leeward side is used in conjunction with the Newtonian methods, $C_P = 0$ on all leeward surfaces.

The second group of windward pressure methods used in this paper are the tangent wedge/cone methods. These methods approximate the panel pressure coefficient to be the same as the pressure coefficient on a wedge/cone of equal inclination. For the tangent wedge method, the pressure coefficient is obtained from the β-θ-M relations and the oblique shock relations as given in Anderson (Equations (4.19)–(4.21)) [19]. First, the shock angle, β, is obtained from the unique functions of Mach Number M and surface inclination θ given by

$$\beta = \tan^{-1} \frac{M^2 - 1 + 2\psi \cos \frac{4\pi\delta + \cos^{-1}\phi}{3}}{3(1 + \frac{\gamma-1}{2} M^2) \tan\theta} \tag{6}$$

where

$$\psi = \sqrt{(M^2-1)^2 - 3\left(1+\frac{\gamma-1}{2}M^2\right)\left(1+\frac{\gamma+1}{2}M^2\right)\tan^2\theta} \tag{7}$$

and

$$\phi = \frac{(M^2-1)^3 - 9\left(1+\frac{\gamma-1}{2}M^2\right)\left(1+\frac{\gamma-1}{2}M^2+\frac{\gamma+1}{4}M^4\right)\tan^2\theta}{\psi^3} \tag{8}$$

In Equation (6), $\delta = 1$ represents the weak shock solution and $\delta = 0$ represents the strong shock solution. In nature, the weak shock solution usually prevails; thus, only the weak shock solution is considered in this paper.

The oblique shock relations provide the surface pressure ratio of a wedge in supersonic or hypersonic flow as

$$\frac{P_2}{P_\infty} = 1 + \frac{2\gamma}{\gamma+1}[(M_\infty \sin\beta)^2 - 1]. \tag{9}$$

The pressure ratio is related to the pressure coefficient by [19]

$$C_{P,\mathrm{TW}} = \frac{2}{\gamma M_\infty^2}\left(\frac{P_2}{P_\infty} - 1\right). \tag{10}$$

If the panel inclination angle produces a shock angle above the maximum shock attachment angle, a detached shock is predicted and the tangent wedge method cannot be used to approximate the pressure coefficient. The modified Newtonian method is then used to calculate the pressure coefficient on such panels. The maximum shock attachment angle is determined based upon the freestream Mach number and specific heat ratio as given by

$$\beta_{\max} = \cos^{-1}\left[\frac{\sqrt{\frac{3M_\infty^2\gamma - \sqrt{(\gamma+1)(8M_\infty^2\gamma + M_\infty^4\gamma - 8M_\infty^2 + M_\infty^4 + 16)} - M_\infty^2 + 4}{\gamma}}}{2M_\infty}\right]. \tag{11}$$

The maximum panel inclination angle can then be obtained from the θ-β-M relation, which is given as

$$\theta_{\max} = \tan^{-1}\left[\left(\frac{2}{\tan\beta_{\max}}\right)\left(\frac{M_\infty^2\sin^2\beta_{\max} - 1}{M_\infty^2(\gamma + \cos 2\beta_{\max}) + 2}\right)\right] \tag{12}$$

Next is the tangent cone method. The solution for the cone pressure coefficient is carried out by solving the Taylor–Maccoll equations for conical flow given as [19]

$$\frac{dV_r}{d\varphi} = V_\varphi \tag{13}$$

and

$$\frac{dV_\varphi}{d\varphi} = \frac{{V_\varphi}^2 V_r - \frac{\gamma-1}{2}\left(1 - {V_r}^2 - {V_\varphi}^2\right)\left(2V_r + V_\varphi\cot\varphi\right)}{\left[\frac{\gamma-1}{2}\left(1 - {V_r}^2 - {V_\varphi}^2\right) - {V_\varphi}^2\right]} \tag{14}$$

The Taylor–Maccoll equation is a system of two first-order ODEs that must be solved numerically. The Taylor–Maccoll equations describe the axisymmetric, inviscid, compressible flow field between a conical shock and a cone surface. The solution procedure is carried out in reverse; first, an arbitrary shock angle is assumed. Then, the Taylor–Maccoll equations are solved, marching inwards from the assumed shock angle. The deflection angle θ is sought where the normal velocity $V_\varphi = 0$. This deflection angle corresponds to the theoretical solid cone angle which supports the assumed shock angle. The surface velocity V_r on the cone

is then known. Oblique shock relations and isentropic relations give the surface pressure coefficient on the cone.

Solving the Taylor–Maccoll equations is computationally expensive. HI-Mach does not directly solve these equations every run. Instead, HI-Mach uses a sixth-order polynomial to represent the cone surface pressure coefficient represented as

$$C_{P,\mathrm{TC}}(\theta) = C_0 + C_1\theta + C_2\theta^2 + C_3\theta^3 + C_4\theta^4 + C_5\theta^5 + C_6\theta^6 \tag{15}$$

The coefficients C_0 through C_6 were calculated and tabulated across a range of freestream Mach numbers and specific heat ratios. When HI-Mach is run with the tangent cone method, the pressure coefficients on a panel with a given inclination are linearly interpolated from the polynomials at the nearest tabulated Mach numbers and specific heat ratios to the flight conditions.

Similar to the tangent wedge method, the Taylor–Maccoll equations cease to yield valid solutions once the shock detaches. This occurs when the cone angle exceeds a critical value, $\theta_{\max}$ This limiting cone angle, $\theta_{\max}$, is determined during the Taylor–Maccoll solution process and stored for interpolation. When a panel inclination is above the cone $\theta_{\max}$ for given flight conditions, another pressure method must be used.

For 90% of panel inclinations, the percent error for the interpolated pressure coefficient is within 2% of the exact pressure coefficient. For panel inclinations with a large relative error, the pressure coefficient is very low. As a result, these panels with high relative error have little impact on the overall aerothermal results. This level of accuracy is judged to be appropriate for a low-fidelity engineering solver.

2.1.3. Leeward Pressure Method

The method for calculating the leeward pressure coefficients used in this paper is a Prandtl–Meyer expansion from the freestream Mach number. The Prandtl–Meyer function is given by

$$\nu(M) = \sqrt{\frac{\gamma+1}{\gamma-1}}\tan^{-1}\left[\sqrt{\frac{\gamma-1}{\gamma+1}(M^2-1)}\right] - \tan^{-1}\left(\sqrt{M^2-1}\right) \tag{16}$$

For conducting analysis using the Prandtl–Meyer function, the inclination angle is related to the Prandtl–Meyer function by

$$\theta = \nu(M) - \nu(M_\infty). \tag{17}$$

This expansion is applied through $\theta_{max} < \theta < 0$. The max turning angle is given by

$$\theta_{\max} = -\left[\frac{\pi}{2}\left(\sqrt{\frac{\gamma+1}{\gamma-1}} - 1\right) - \nu(M_\infty)\right] \tag{18}$$

Beyond the max turning angle, the flow is considered as separated. The pressure is then determined using the base region relations shown later. Solving the Prandtl–Meyer function yields the Mach number at the expansion surface of inclination θ. The pressure coefficient on the expansion surface is given as

$$C_{P,\mathrm{PM}} = \frac{2}{\gamma M_\infty^2}\left[\left(\frac{1+\frac{\gamma-1}{2}M_\infty^2}{1+\frac{\gamma-1}{2}M^2}\right)^{\frac{\gamma}{\gamma-1}} - 1\right] \tag{19}$$

At the start of each run, the Prandtl–Meyer function is solved numerically across a range of Mach numbers, and the resulting $M(\nu)$ relationship is tabulated for efficient lookup during panel evaluation.

2.1.4. Base Region

This paper uses two pressure methods that can be used to calculate the pressure coefficient in the base regions of the body where flow is separated. The first is the vacuum pressure coefficient given by [10]

$$C_{P,\text{Vacuum}} = \frac{-2}{\gamma M_\infty^2} \tag{20}$$

The second is Gaubeaud's formula given by [10]

$$C_{P,\text{Gaubeaud}} = \frac{2}{\gamma M_\infty^2}\left[\left(\frac{2}{\gamma+1}\right)^{1.4}\left(\frac{1}{M_\infty}\right)^{2.8}\left(\frac{2\gamma M_\infty^2-(\gamma-1)}{(\gamma+1)}\right)-1\right] \tag{21}$$

2.2. Viscous Aerodynamics

The calculation of the skin friction forces in HI-Mach consists of determining the boundary layer edge properties, tracing streamlines, and relating these values to the local skin friction coefficient. This section presents the calculation of the surface properties and the skin friction coefficient. The process for tracing streamlines is of much greater complexity and thus given in the following section.

2.2.1. Thermodynamic Properties

Once the pressure coefficient is obtained, the remaining thermodynamic properties for skin friction calculations are calculated. To calculate these properties, it may be assumed that all flow on the edge of the boundary layer either passes through a normal or oblique shock and is isentropic post-shock. In most cases, a normal shock is assumed. However, there are some special cases in which the shock angle is known, such as conically derived waveriders, and the oblique shock relations may prove useful. The following relations are derived using the normal shock, oblique shock, and isentropic ideal gas relations provided by Anderson [20]. The pressure on a surface face i is given by

$$P_i = P_\infty\left(\frac{C_{P,i}\gamma M_\infty^2}{2}+1\right) \tag{22}$$

Because the boundary layer is thin, it is assumed that the pressure does not vary throughout the boundary layer in the direction normal to the surface. Therefore, the pressure at the boundary layer edge is equal to the pressure at the surface,

$$P_{e,i} = P_i. \tag{23}$$

From the surface pressure, the Mach number at the edge of the boundary layer at surface element i can be defined by

$$M_{e,i} = \sqrt{\frac{2}{\gamma-1}\left(\left(\frac{P_0}{P_{e,i}}\right)^{\frac{\gamma-1}{\gamma}}-1\right)} \tag{24}$$

where P_0 is the post-shock stagnation pressure. Using the normal shock relations, P_0 is related to the freestream conditions by

$$P_0 = P_\infty \left[\frac{(\gamma+1)^2 M_\infty^2}{4\gamma M_\infty^2 - 2(\gamma-1)} \right]^{\frac{\gamma}{\gamma-1}} \frac{1-\gamma+2\gamma M_\infty^2}{\gamma+1} \tag{25}$$

Using the oblique shock relations, P_0 is related to the freestream conditions by

$$P_0 = P_\infty \left[1 + \frac{2\gamma}{\gamma+1} \left(M_\infty^2 \sin^2\beta - 1 \right) \right] \left[1 + \frac{\gamma-1}{2} M_2^2 \right]^{\gamma/(\gamma-1)} \tag{26}$$

where M_2 is the post-shock Mach number given by

$$M_2 = \left\{ \sqrt{\frac{1 + [(\gamma-1)/2] M_\infty^2 \sin^2\beta}{\gamma M_\infty^2 \sin^2\beta - (\gamma-1)/2}} \right\} / \sin(\beta - \theta) \tag{27}$$

where θ is the deflection angle of the surface generating the shock. The boundary layer edge temperature at a surface element i can then be defined by

$$T_{e,i} = T_0 \frac{2}{2 + (\gamma-1) M_{e,i}^2} \tag{28}$$

where T_0 is the stagnation temperature post shock. Because the total temperature is conserved across a shock for a calorically perfect, non-reacting gas, the post-shock stagnation temperature may be taken as the freestream stagnation temperature

$$T_0 = T_\infty \left(1 + \frac{\gamma-1}{2} M_\infty^2 \right) \tag{29}$$

The magnitude of the velocity on the edge of the boundary layer is given by

$$V_{e,i} = M_{e,i} \sqrt{\frac{\gamma R_U T_{e,i}}{m_{\text{mol}}}} \tag{30}$$

where R_U is the universal gas constant and m_{mol} is the molar mass of the gas. The density at the edge of the boundary layer is given by

$$\rho_{e,i} = \frac{P_{e,i}\, m_{\text{mol}}}{R_U\, T_{e,i}} \tag{31}$$

The dynamic viscosity on the edge of the boundary layer is calculated using Sutherland's law [21], which is given by

$$\frac{\mu}{\mu_{\text{ref}}} \approx \left(\frac{T}{T_{\text{ref}}} \right)^{3/2} \frac{T_{\text{ref}} + S}{T + S} \tag{32}$$

where μ_{ref} and T_{ref} are reference values and S is the Sutherland constant, which is a characteristic of the gas. For air $\mu_{\text{ref}} = 1.716\text{E}-5$ N· s/m^2, $T_{\text{ref}} = 273$ K, and $S = 111$ K. Reference values for other common gases can be found in textbooks [21]. Sutherland's law is found to be accurate to ±2% from 170 K to 1900 K.

2.2.2. Reference Temperature

The reference temperature provides an effective mean temperature in the boundary layer. The fluid properties are evaluated at this reference temperature when applying incompressible flat-plate skin-friction correlations to compressible boundary layers. Two

reference temperature methods are implemented in this paper: the Eckert and the Meador–Smart formulations. The Eckert reference temperature is given by [22]

$$\frac{T^*}{T_e} = 1 + 0.032M_e^2 + 0.58\left(\frac{T_w}{T_e} - 1\right) \tag{33}$$

where T_e is the boundary layer edge temperature and T_w is the wall temperature.

The Meador–Smart reference temperature method [23] uses different formulas for laminar and turbulent flow. For laminar flow, the reference temperature is given by

$$\frac{T^*}{T_e} = 0.45 + 0.55\frac{T_w}{T_e} + 0.16r\left(\frac{\gamma - 1}{2}\right)M_e^2 \tag{34}$$

where r is the recovery factor, which for laminar flow $r = \sqrt{Pr}$. For turbulent flow, the reference temperature is given by

$$\frac{T^*}{T_e} = 0.5\left(1 + \frac{T_w}{T_e}\right) + 0.16r\left(\frac{\gamma - 1}{2}\right)M_e^2 \tag{35}$$

where for turbulent flow, $r = (Pr)^{1/3}$. The Prandtl number of air is assumed to be $Pr = 0.71$. The wall temperature depends on the specific wall condition used. These conditions are described in Section 2.6.

2.2.3. Skin Friction

For laminar flow, the skin friction coefficient is given as [4]

$$c_{f_L}^* = \frac{0.664}{\sqrt{Re_x^*}} \tag{36}$$

For turbulent flow, the skin friction coefficient is given as [4]

$$c_{f_T}^* = \frac{0.0592}{(Re_x^*)^{0.2}} \tag{37}$$

However, Meador and Smart recommend using [23]

$$c_{f_T}^* = \frac{0.02296}{(Re_x^*)^{0.139}} \tag{38}$$

for turbulent flow with their reference temperature method. In the above equations, Re_x^* is the running length Reynolds number evaluated at the reference temperature. The process for determining Re_x^* is given in the following section on streamlines.

This paper utilizes a local Mach number correlation to approximate the transition Reynolds number [24]. This correlation is useful because the local Mach number can be obtained directly from the normal shock relations and impact methods. The transition criteria is given by

$$\log_{10}(Re_T) = 6.421\ \exp[1.209 \times 10^{-4}M_e^{2.641}] \tag{39}$$

If $Re_x^* > Re_T$ then the flow is considered transitional and the skin friction is given by [24]

$$c_{f_{TR}}^* = (1 - \Gamma)c_{f_L}^* + \Gamma c_{f_T}^* \tag{40}$$

where

$$\Gamma(x) = 1 - e^{-3\left\{exp\left[\frac{\ln 2}{5x_{TR}}(Re_x)_T^{0.2}(x - x_{TR})\right] - 1\right\}^2} \tag{41}$$

where x is the current running length and x_{TR} is the running length at transition. Turbulent transition is a notoriously difficult phenomenon to predict. The transition model proposed here should serve as an indicator of when transition might happen and not an exact prediction of transition. Several factors that affect transition are not included in this model such as surface roughness and pressure gradients.

2.3. Streamlines and Running Length

One necessary part of calculating the skin friction coefficient is finding the running length Renoylds number given as

$$Re_x^* = \frac{\rho^* V_e x}{\mu^*} \tag{42}$$

where x is the running length, which is calculated as the streamline distance from the beginning of the boundary layer to the panel of interest. To calculate the running length, a velocity distribution is first established on the body. Then, the attachment regions where the boundary layer begins are identified, and streamlines are traced.

2.3.1. Velocity Distribution

The velocity direction at the center of each panel is taken as the projection of the freestream direction onto the local surface tangent plane given by [8,25,26]

$$\frac{\boldsymbol{V_i}}{|\boldsymbol{V_i}|} = \frac{\hat{\boldsymbol{n}}_i \times \hat{\boldsymbol{V}}_\infty \times \hat{\boldsymbol{n}}_i}{|\hat{\boldsymbol{n}}_i \times \hat{\boldsymbol{V}}_\infty \times \hat{\boldsymbol{n}}_i|} \tag{43}$$

where $|\boldsymbol{V_i}|$ is the velocity magnitude given by Equation (30). A linear velocity distribution on the surface of each panel, which is important for finding attachment lines and surface streamlines, may then be calculated. The local velocity distribution on each panel will take the form [27]

$$\begin{Bmatrix} u^l \\ v^l \end{Bmatrix} = \begin{Bmatrix} a_1 \\ a_2 \end{Bmatrix} + \begin{bmatrix} b_1 & c_1 \\ b_2 & c_2 \end{bmatrix} \begin{Bmatrix} x^l \\ y^l \end{Bmatrix} \tag{44}$$

where x^l and y^l are the local panel coordinates. A vector can be rotated into local coordinates by the transformation

$$\boldsymbol{x}^l = [A_{g \to l}]\boldsymbol{x} \tag{45}$$

where $[A_{g \to l}]$ is an orthogonal matrix consisting of two orthogonal vectors in the plane of the panel and the normal vector. In this paper, the orthogonal vectors are chosen to be the velocity direction vector and a vector perpendicular to it and the normal vector. The process for calculating the coefficients in (44) is described in [1].

2.3.2. Attachment Lines

Attachment lines determine the panels on the mesh where the streamlines begin and from which the running length is calculated. This paper follows the methods of Kenwright [27,28] to identify attachment lines. Differentiating Equation (44) and algebraically manipulating the resulting equations results in a pair of second-order non-homogenous ODEs. If the determinant of the Jacobian matrix is non-zero, the solution takes the form

$$\begin{Bmatrix} x(t) - x_{cp} \\ y(t) - y_{cp} \end{Bmatrix} = \begin{bmatrix} \xi_1 & \eta_1 \\ \xi_2 & \eta_2 \end{bmatrix} \begin{Bmatrix} B_1 e^{\lambda_1 t} \\ B_2 e^{\lambda_2 t} \end{Bmatrix} \tag{46}$$

where λ_1 and λ_2 are the eigenvalues of the Jacobian matrix and $\{\xi_1, \xi_2\}^T$ and $\{\eta_1, \eta_2\}^T$ are the associated eigenvectors. The constants B_1 and B_2 define a particular curve in the phase plane. The constants x_{cp} and y_{cp} correspond to the location of the critical point given by

$$x_{cp} = \frac{a_2 c_1 - a_1 c_2}{b_1 c_2 - b_2 c_1} \tag{47}$$

$$y_{cp} = \frac{a_1 b_2 - a_2 b_1}{b_1 c_2 - b_2 c_1} \tag{48}$$

These constants (x_{cp} and y_{cp}) translate the coordinate system such that the origin coincides with the critical point. Every triangle will have a critical point somewhere in its linear velocity field; however, the critical point will not generally lie inside the triangle. Matters are simplified by transforming to the phase plane where the eigenvectors are orthogonal using

$$\begin{Bmatrix} X \\ Y \end{Bmatrix} = \begin{bmatrix} \xi_1 & \eta_1 \\ \xi_2 & \eta_2 \end{bmatrix}^{-1} \begin{Bmatrix} x - x_{cp} \\ y - y_{cp} \end{Bmatrix} = \begin{Bmatrix} B_1 e^{\lambda_1 t} \\ B_2 e^{\lambda_2 t} \end{Bmatrix} \tag{49}$$

The triangle vertices are transformed into the canonical coordinate system using Equation (49). Attachment and separation lines are identified on the triangle if the triangle straddles the X-axis or Y-axis. In this paper, only attachment lines are of interest. The phase portrait of the velocity field is determined using eigenvalue tests. If $\lambda_2 < 0 < \lambda_1$ or $0 < \lambda_2 < \lambda_1$ and the triangle straddles the Y-axis, the triangle contains an attachment line. The direction of that attachment line is given by the eigenvector $\{\eta_1, \eta_2\}^T$.

This attachment line method works well for identifying attachment lines on the surface of smooth, blunt geometries. Figure 2 shows the panels containing attachment lines at the nose, wings, and chines of the HL-20. However, this attachment line method does not accurately detect attachment lines on sharp leading edges. These undetected attachment lines are identified during the streamline integration process.

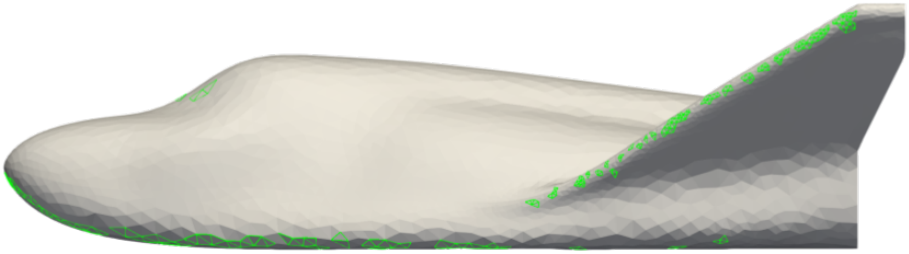


Figure 2. Detected attachment line panels (highlighted in green) on HL-20 at 25° angle of attack. Reprinted with permission from Goates et al. [1]. Copyright ©2025 Goates.

Once attachment lines have been detected, a smoothing algorithm is run to ensure a smooth solution in the case of irregular meshing. This is accomplished by checking the number of attachment lines surrounding each panel. If the proportion of surrounding panels that contain attachment lines is greater than 0.6, the panel of interest is identified as an attachment line panel. If a panel contains an attachment line but none of the surrounding panels do, the panel is treated as a normal panel without an attachment line.

2.3.3. Surface Streamlines

This paper uses both analytical and numerical methods to trace a streamline along the surface of the geometry. Streamlines are necessary for finding the running length used to calculate the local Reynolds number of the flow. Because the velocity is only defined on the

surface of the geometry, a panel-to-panel streamline method is used to trace a streamline backwards from each panel to its attachment line panel of origin.

The streamline first begins on the centroid of a panel. The path of that streamline along the panel surface is parameterized and is given by Equation (46). This analytic expression is valid because the local velocity field is approximated as linear over each panel. The eigenvectors and eigenvalues for each panel were calculated previously during the attachment line analysis and are stored to decrease the computational cost of finding the surface streamlines. The constants B_1 and B_2 are found by setting $t = 0$ in Equation (46). The resulting expression is

$$\begin{Bmatrix} B_1 \\ B_2 \end{Bmatrix} = \begin{bmatrix} \xi_1 & \eta_1 \\ \xi_2 & \eta_2 \end{bmatrix}^{-1} \begin{Bmatrix} x(0) - x_{cp} \\ y(0) - y_{cp} \end{Bmatrix} \tag{50}$$

It is important to note that the inverse eigenvector matrix was also calculated during the attachment line analysis and is stored for each panel, allowing for a further decrease in computational cost.

The position of the streamline is calculated along discrete time steps. At each time step, the location is transformed into barycentric coordinates. The barycentric coordinates are defined as the solution to the linear system

$$[R] \begin{Bmatrix} \Lambda_1 \\ \Lambda_2 \\ \Lambda_3 \end{Bmatrix} = \begin{Bmatrix} 1 \\ x \\ y \end{Bmatrix} \tag{51}$$

where

$$[R] = \begin{bmatrix} 1 & 1 & 1 \\ x_1 & x_2 & x_3 \\ y_1 & y_2 & y_3 \end{bmatrix} \tag{52}$$

where the coordinates x and y are in the local coordinate system. The barycentric coordinate transform is then given by

$$\begin{Bmatrix} \Lambda_1 \\ \Lambda_2 \\ \Lambda_3 \end{Bmatrix} = [R]^{-1} \begin{Bmatrix} 1 \\ x \\ y \end{Bmatrix} \tag{53}$$

where

$$[R]^{-1} = \frac{1}{2A} \begin{bmatrix} x_2y_3 - x_3y_2 & y_2 - y_3 & x_3 - x_2 \\ x_3y_1 - x_1y_3 & y_3 - y_1 & x_1 - x_3 \\ x_1y_2 - x_2y_1 & y_1 - y_2 & x_2 - x_1 \end{bmatrix} \tag{54}$$

$$2A = x_1(y_2 - y_3) + x_2(y_3 - y_1) + x_3(y_1 - y_2). \tag{55}$$

If the point is inside the triangle, all the barycentric coordinates will be between 0 and 1. This transformation allows for an easy recognition of when and where the streamline has left the panel boundary. When the streamline exits the panel, the crossing edge is identified and the intersection of the chord joining the last two streamline points with that edge is computed by

$$\hat{x}_i = -\Lambda_j(\hat{x}_{out}) \frac{\hat{x}_{in} - \hat{x}_{out}}{\Lambda_j(\hat{x}_{in}) - \Lambda_j(\hat{x}_{out})} + \hat{x}_{out} \tag{56}$$

where $\hat{x}_i$ is the panel streamline end point and Λ_j is the barycentric coordinate related to the intersection edge. The streamline is then transferred to the neighboring panel sharing that edge and continued from the intersection point. The streamline is continued along the surface of that panel using the same procedure as before.

The panel-wise streamline integration is continued until the streamline reaches a panel containing an attachment line, at which point the running length of the streamline and its attachment line panel of origin are stored. If a streamline is passed back and forth between two panels, HI-Mach recognizes this as a sharp leading edge and will classify those two panels as attachment line panels. The running length of the streamline is calculated as the sum of the distances between the entrance and exit points on each panel.

Streamline integration can become a computationally expensive process when compared to the other computations in HI-Mach. To lower the computational cost of integrating streamlines, a sparse method may be used. This method ensures that only one streamline passes through each panel. As a streamline is integrated, the length of that streamline is stored for each panel that it passes through. The integration continues until it reaches an attachment line or a panel where the streamline has already been calculated. Streamlines using both the sparse method and the full calculation can be seen in Figure 3. Figure 4 displays the difference in the resulting running length calculations. Use of the sparse streamline method on the HL-20 geometry resulted in a three-fold speed up. The error introduced by use of the sparse method is shown in Figure 5. A maximum error of 1.7% in the viscous drag coefficient was observed for the cases considered.

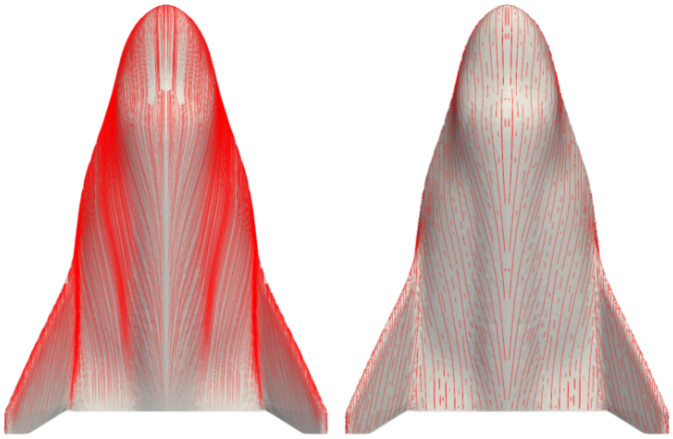


Figure 3. Surface streamline patterns on the body of HL-20 at 25° angle of attack. ((**Left**): Full Streamlines, (**Right**): Sparse Streamlines.) Reprinted with permission from Goates et al. [1]. Copyright ©2025 Goates.

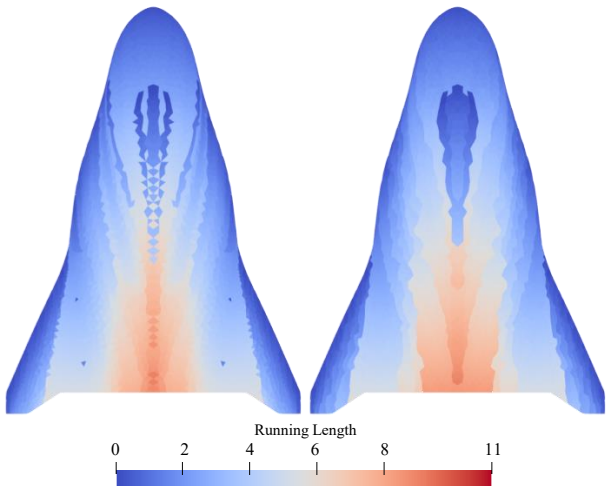


Figure 4. Running lengths, $x = (m)$, on the body of HL-20 at 25° angle of attack. ((**Left**): Full Streamlines, (**Right**): Sparse Streamlines.) Adapted with permission from Goates et al. [1]. Copyright ©2025 Goates.

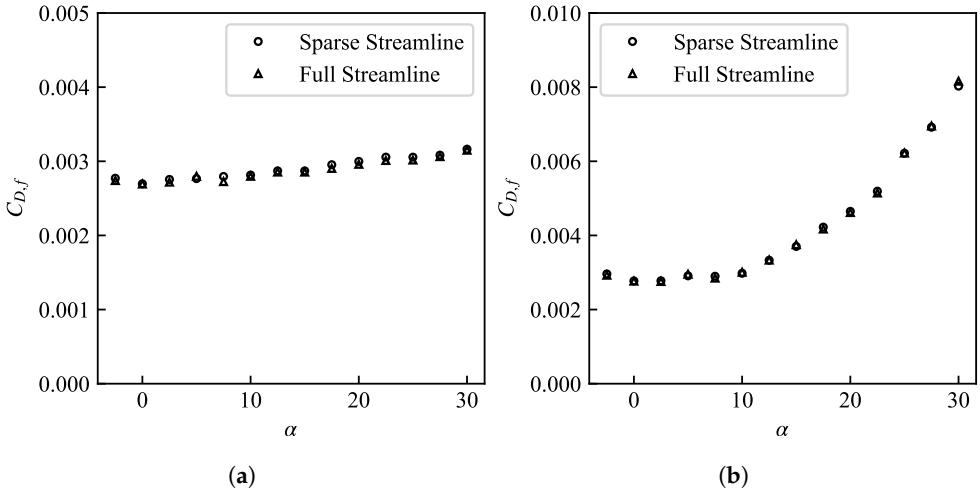


Figure 5. Comparison of viscous drag coefficients for varying α in degrees between the sparse and full streamline methods on the HL-20. (**a**) $M_\infty = 1.6$; (**b**) $M_\infty = 4.5$.

2.4. Convective Heating

In hypersonic flow, Newtonian impact theory can be used to predict surface pressure coefficients with reasonable accuracy [4]. The assumption of isentropic post-shock flow and a thin boundary layer also gives expressions for the velocity, temperature, and pressure on the edge of the boundary layer based on the surface pressure as described previously. Based on the theory, there are two procedures for calculating the convective heating on the surface. One is for stagnation and attachment line regions, and the other is for any regions outside of a stagnation or attachment region. Radiative heating from the boundary layer to the surface is not considered in this paper.

2.4.1. Stagnation and Attachment Line Heating

Based on the assumptions that the boundary layer pressure gradient and thickness are small, it is possible to obtain an analytical form for stagnation heat transfer. Fay and Riddell [29] derived forms for the heat transfer in a spherical or cylindrical stagnation region using a self-similar boundary layer solution. The local curvature ratio κ_1/κ_2 is used as a geometric weighting factor when considering elliptic attachment regions.

Under the assumption that the Lewis Number Le = 1, the following forms for stagnation line heat transfer to a sphere or cylinder were obtained from the Fay–Riddell solutions by Tauber [30].

The formula for stagnation heating can be generalized so that it is not unique to a sphere or cylinder. The heat flux to the wall $\dot{q}_w$ can be given as

$$\dot{q}_w = k_{\text{geom}}(h_{aw} - h_w)\text{Pr}_{wf}^{-0.6}(\rho_w\mu_w)^{0.07}(\rho_e\mu_e)^{0.43}\left(\frac{du_e}{dx}\right)^{0.5} \tag{57}$$

where k_{geom} is the geometric factor given by

$$k_{\text{geom}} = 0.768\sqrt{\frac{1+\frac{R_1}{R_2}}{2}} \tag{58}$$

The term R_1/R_2 is the ratio of the radius of curvature in the direction perpendicular to the attachment line to the radius of curvature in the attachment line direction. The attachment line detection methods and ordering of R_1 and R_2 ensure that this ratio is always between 0 and 1. The term $(h_{aw} - h_w)$ is the wall enthalpy difference and is discussed later. For

a cylinder, stagnation heating decreases with the sweep angle, Λ. One option to account for the effects of sweep is to use a modified expression for the velocity gradient and a modified expression for the adiabatic wall temperature which account for the effects of sweep. Alternatively, a general scaling factor can be applied to account for the effects of sweep in both the velocity gradient and adiabatic wall temperature. The general scaling factor is the method used in this paper.

Multiple correlated forms for the general sweep scaling factor are available in the literature. Tauber [30] proposes the following

$$\frac{\dot{q}_\Lambda}{\dot{q}_{\Lambda=0}} = \cos\Lambda\left(1 - 0.18\sin^2\Lambda\right) \tag{59}$$

The dependence on sine in Tauber's correlations results from induced spanwise flow at sufficiently large sweep angles.

Other methods were considered in [2]. The examined experimental results indicate that Tauber's method best captures the variation in heating rate with sweep angle. For this reason, Tauber's method is used in the this paper to account for swept attachment lines.

The surface-parallel velocity gradient $\frac{du_e}{dx}$ is used in the calculation of the convective heating. Three approaches to determine the velocity gradient are discussed here. Theoretical calculations of stagnation heating performed with the Newtonian velocity gradient tend to underpredicting wind-tunnel or flight-tested measurements of stagnation heating. Olivier attributed this to the velocity gradient being too low [31]. Based on shock and boundary layer theory, Olivier derived an analytical result for the velocity gradient given by

$$\frac{du_e}{dx} = \frac{u_\infty}{R}\frac{1+\bar{\Delta}}{\bar{\Delta}}\frac{P_0 - P_2}{\rho_\infty u_\infty^2}\frac{\rho_2}{\rho_s} \tag{60}$$

where the non-dimensional shock standoff distance $\bar{\Delta}$ can be obtained from correlated relations for a sphere obtained by Billig [32] and given by

$$\bar{\Delta} = \frac{\Delta}{R} = 0.143e^{\frac{3.24}{M_\infty^2}} \tag{61}$$

The second and most common method to calculate the velocity gradient is derived from the assumption of a Newtonian pressure distribution [4]. Analysis yields

$$\frac{du_e}{dx} = \frac{1}{R}\left[\frac{4(P_e - P_\infty)}{C_{p,\max}\rho_e}\right]^{\frac{1}{2}} \tag{62}$$

where $C_{p,\max}$ is 2 for the Straight Newtonian method or a calculated value for the Modified Newtonian method. The third method is an alternate form for the velocity gradient given by DeJarnette [33] as

$$\frac{du_e}{dx} = \frac{|u_\infty|}{R}\sqrt{1.85\frac{\rho_\infty}{\rho_e}} \tag{63}$$

The square root of the velocity gradient is calculated and plotted in Figure 6 using these relations. The DeJarnette and Modified Newtonian solutions produce heating rates approximately 10% lower than Olivier's method. Olivier demonstrated that his method matches wind tunnel and flight-measured heating rates better [31]. For this reason, the Olivier velocity gradient is implemented as the default option for HI-Mach.

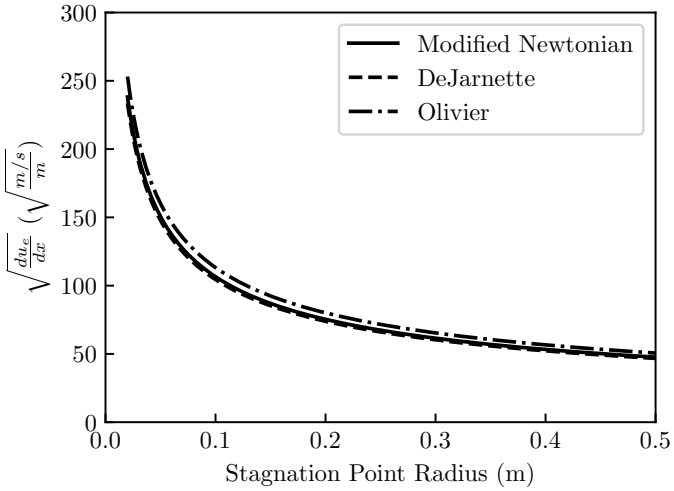


Figure 6. Comparison of calculated velocity gradients at Mach 10.0, $P_\infty = 10$ kPa, $\rho_\infty = 0.1$ kg/m^3. Reprinted with permission from Freeman et al. [2]. Copyright ©2025 Freeman.

The enthalpy difference between adiabatic wall and wall conditions $h_{aw} - h_w$ is the driving factor for convective heat transfer. The adiabatic wall enthalpy is determined from the adiabatic wall temperature T_{aw}, which is in turn determined using the recovery factor. For a spherical stagnation point, the recovery factor is taken to be 1, yielding $T_{aw} = T_0$. On a general cylindrical stagnation line, the recovery factor depends on the sweep angle [34]. However, because this paper includes a general scaling factor to account for the effects of sweep, the recovery factor on a cylinder is also taken to be 1.

2.4.2. Acreage Heating

The heating across the majority of the body is calculated using general incompressible flat-plate solutions corrected for compressibility and geometry. The skin friction coefficient, c_f^*, is related to the heat transfer coefficient, $\overline{C_H}^*$, by the Reynolds analogy [4]

$$\overline{C_H}^* = \frac{c_f^*}{2s} \tag{64}$$

where s is the Reynolds analogy factor, which is given as

$$s = (\mathrm{Pr}^*)^{2/3} \tag{65}$$

By assuming that the Prandtl number for laminar and turbulent flow is the same, $\mathrm{Pr} = 0.71$ for this paper, Equation (65) applies to both laminar and turbulent flow. For a more detailed discussion of the Reynolds analogy factor, see [35]. The use of the Reynolds analogy assumes that the thermal and momentum boundary layers begin at the same location. In cases where there is a large temperature gradient along the boundary layer, the present methods would be expected to perform poorly. Future work could include the effects of streamwise pressure and temperature gradients for increased fidelity. The heat transfer rate to the surface is given as

$$\dot{q}_w = \rho^* u_e (h_{aw} - h_w) \overline{C_H}^* \tag{66}$$

To account for the three-dimensional relieving effects of surface curvature, a Mangler factor M_f is applied to the friction coefficient when the local curvature ratio κ_1/κ_2 indicates a significant deviation from flat-plate conditions. Following Tauber [30], $M_f = \sqrt{3}$ is used for laminar flow and $M_f = 1.15$ for turbulent flow. The corrected coefficient is $c_f^* = M_f c_{f,\mathrm{flat}}^*$.

2.4.3. Blending of Heating Methods

After stagnation and attachment line heating calculations are performed, a running length offset is applied. This is calculated by

$$\dot{q}_{\text{acreage},x_0} = \dot{q}_{\text{attachment}} \tag{67}$$

where $\dot{q}_{\text{acreage},x_0}$ is the heating at some running length offset x_0. The running length on all panels having streamlines originating from the attachment line panel are offset by x_0. This process allows for a continuous and smooth solution, ensuring that the downstream neighbors of a stagnation or attachment panel have the correct heat flux. The solution is further smoothed by taking a local average of $\dot{q}_{\text{attachment}}$ that includes the neighbor panels of the streamline origin.

2.5. Mesh Curvature Methods

The surface curvature of the mesh is used in calculating the heating solution. For stagnation and attachment line regions, the velocity gradient is determined based on the local radius of curvature. For acreage regions, the local ratio of curvatures is used to apply the Mangler correction factor for three-dimensional effects. In addition, the local surface curvature can be used to automatically choose an aerodynamic method to apply to a panel. For example, the tangent wedge method would be appropriate on a region with low local surface curvature, and the tangent cone method would be appropriate on a region with higher local surface curvature. This saves the user considerable time and effort from manually setting the aerodynamic methods on a mesh.

Heating calculations are made on a per-panel basis to determine the convective heat flux into a panel. Therefore, the local surface curvature is desired at every panel. The curvature is represented by the shape operator, $\boldsymbol{S}$. For a three-dimensional mesh, the shape operator is a second-order tensor which represents the rate of change of the normal vector. The maximum and minimum radii of curvature and directions of maximum and minimum curvature can be obtained from the shape operator. The goal of these curvature methods is to obtain an approximation for the shape operator.

Two methods for estimating the shape operator are implemented in HI-Mach: a local paraboloid-fitting method and a difference-of-normals method. Their application is described in detail in [2]. When the shape operator $\boldsymbol{S}$ on a face is known, the curvatures and curvature directions are easy to calculate. The minimum and maximum curvatures, κ_1 and κ_2 are the eigenvalues of $\boldsymbol{S}$, and the minimum and maximum curvature directions, $\boldsymbol{\xi}_1$ and $\boldsymbol{\xi}_2$, are the eigenvectors of $\boldsymbol{S}$.

$$\kappa_1, \kappa_2 = \text{eigval}(\boldsymbol{S}) \tag{68}$$

$$\boldsymbol{\xi}_1, \boldsymbol{\xi}_2 = \text{eigvec}(\boldsymbol{S}) \tag{69}$$

The curvature directions are expressed in the panel tangent coordinate system. To transform them back to Cartesian space, the following transformation can be used

$$\boldsymbol{\xi}_{XYZ} = \begin{bmatrix} \boldsymbol{\zeta}_p & \boldsymbol{\vartheta}_p \end{bmatrix} \boldsymbol{\xi}_{\zeta,\vartheta} \tag{70}$$

In practice, the curvature is desired in directions other than the directions of minimum and maximum curvature. In this case, the angle θ between the maximum curvature and the desired direction (which should be on the tangent plane) is computed. Then, Euler's formula is used to compute the directional curvature given as

$$\kappa_n = \kappa_1 \cos^2\theta + \kappa_2 \sin^2\theta \tag{71}$$

where θ is the angle between the arbitrary direction and ξ_1, which is the first principal direction. In calculations where curvature is useful, the desired quantity is usually the radius of curvature. This can be computed as the inverse of the surface curvature given as

$$R = \frac{1}{\kappa}. \tag{72}$$

Grid refinement studies were conducted on spheres and cylinders to evaluate the performance of the curvature calculations. The first study was conducted on a sphere for which the curvature everywhere is equal to the inverse of the radius. The relative error against the true curvature value is plotted in Figure 7.

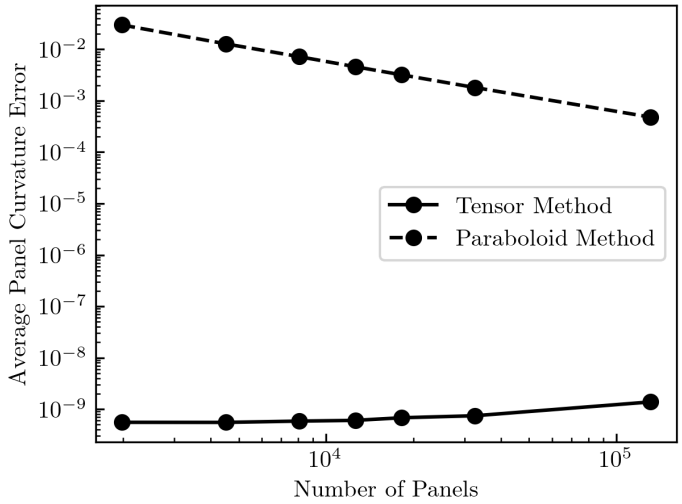


Figure 7. Error in average panel, $\kappa = (1/m)$, for a sphere. Reprinted with permission from Freeman et al. [2]. Copyright ©2025 Freeman.

A similar verification study was conducted on a cylinder. The first principal curvature on a cylinder is equal to the inverse of the cylinder radius. The second principal curvature is 0. The relative errors against these values are plotted in Figure 8.

For both spheres and cylinders, the tensor method displays better overall results for the accuracy of curvature calculations. In the middle of the cylinder, the tensor method always perfectly captures the curvature. However, around the ends of the cylinder, the tensor method has trouble especially with coarse meshes. The paraboloid method displays roughly first-order convergence. The tensor method converges rapidly and exhibits negligible improvement beyond a moderate mesh resolution, suggesting it reaches a discretization-independent accuracy limit. HI-Mach uses the tensor method by default. There are rare circumstances in which the tensor method will fail due to an ill-conditioned or singular system of equations. This usually happens with high aspect ratio panels and sharp edges. If the tensor method fails to calculate the curvature on a panel, the paraboloid method is used as a reliable but less accurate backup.

Robustly calculating the curvature on cylinders and spheres is important, because wing leading edges resemble cylinders, and blunt stagnation points resemble spheres. Accurate curvature calculations are essential for characterizing body regions and determining stagnation heating rates. All methods for calculating curvature based on a discrete mesh are sensitive to mesh quality. Meshes with high aspect ratio triangles or triangles with neighbors that are very different in size are very sensitive, and curvature can be inaccurate in this region. Regions of high interest should be modeled with high triangle density in order to capture the curvature correctly. These regions should include stagnation regions and wing or fin leading edges.

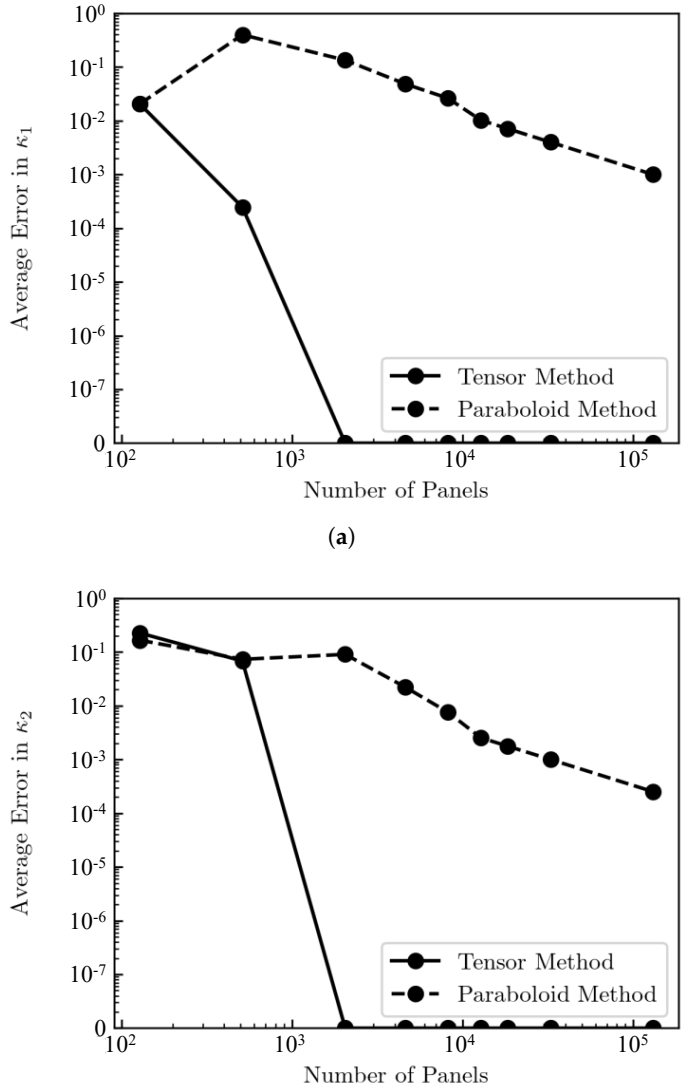


Figure 8. Error in average curvature, $\kappa = (1/m)$, for a cylinder. (**a**) First principal curvature, (**b**) second principal curvature. Reprinted with permission from Freeman et al. [2]. Copyright ©2025 Freeman.

2.6. Wall Conditions

Different wall conditions are implemented in HI-Mach. Each wall condition is appropriate for a different situation. The simplest wall condition is a cold wall, where the user sets the wall temperature. This corresponds to a situation where a vehicle has just entered a hypersonic flowfield, such as in a wind tunnel. This condition also corresponds with a situation where an active cooling system maintains vehicle walls at a given temperature.

The next wall condition is an adiabatic wall. For this wall condition, no heat transfer takes place between the flowfield and the wall. This condition requires that $T_w = T_{aw}$, where T_{aw} is calculated as described earlier. This wall condition is an overprediction of wall temperature and is physically unrealistic. However, the adiabatic wall condition is useful idealization and is implemented for use in comparisons with existing numerical results that used an adiabatic wall.

A third wall condition is radiation equilibrium. In this condition, the convective heat flux into the wall is equal to the radiative heat flux out of the wall. The user specifies the wall emissivity, which yields a simple equilibrium equation for T_w given as

$$\epsilon_w \sigma T_w^4 - C_H(T_{aw} - T_w) = 0. \tag{73}$$

This quartic equation is solved for T_w. However, the heat transfer coefficient C_H is weakly a function of the wall temperature, because it depends on gas properties at the wall. Therefore, this equation must be solved iteratively to converge on the right value for T_w.

The final wall condition is a one-dimensional transient condition. This wall condition has specific application when considering hypersonic trajectories. HI-Mach was developed in parallel with a hypersonic trajectory analysis code [15]. Heat transfer throughout a trajectory is an inherently transient phenomenon. As a vehicle enters the hypersonic regime, its outer skin will heat up and heat will conduct internally into the vehicle. HI-Mach computes a steady-state aerodynamic and heating solution. A trajectory is represented by a series of steady-state solutions, each representing a finite time step during the trajectory. The transient conduction wall condition assumes that the heat flux into the wall is constant during the time step and propagates the internal temperature distribution forward by the required time step. This wall condition is described in detail in [2].

2.7. Sensitivities

In a design and optimization process, the gradient or sensitivity of a quantity is frequently sought. The sensitivity of a desired functional such as lift or drag is generally expressed with respect to some set of parameters. For example, in the optimization of a parametrized airfoil shape, the sensitivity of lift with respect to camber and chord length guides the optimizer to camber and chord lengths that will result in increased lift. Generally, an analysis code with sensitivity capability outputs the sensitivity of a functional with respect to all the points on a discretized geometry. A Computer-Aided Design tool such as Engineering Sketch Pad converts the sensitivity with respect to the geometry to the sensitivity with respect to the parameters [36].

Multiple approaches are commonly used to compute the sensitivities of a functional with respect to the geometry in analysis codes. Detailed discussions of these sensitivity calculation methods are given by Peter and Dwight [37] and Martins and Hwang [38]. A brief review is given here. The simplest approach is using finite differencing to approximate the sensitivity. An initial solution is obtained, the inputs are perturbed, and a new solution is obtained. The estimate of the sensitivity is obtained as a function of the change in the solution and perturbation size. For example, in central-differencing, the sensitivity is estimated as

$$f'(x) \approx \frac{f(x+h) - f(x-h)}{2h} \tag{74}$$

which requires two function evaluations for each estimate of the derivative. This approach works well to calculate the sensitivities with respect to a few parameters. However, calculating the shape sensitivities of a geometry requires calculating the sensitivity of each vertex in each of the three coordinate directions. Therefore, calculating the shape sensitivity using central-differencing requires evaluating the solution $6n$ times, where n is the number of vertices making up a geometry. This is prohibitively expensive for large geometries. The central difference method also has limited accuracy due to round-off and truncation error. With very small step sizes, subtractive cancellation or round-off error reduces the accuracy of the method. For large step sizes, the truncation error dominates. The trade-off between round-off and truncation error is described by Kenway [39].

An alternative to traditional finite-difference methods is the complex-step approximation. The general form is

$$f'(x) \approx \text{imag}\left(\frac{f(x+hi)}{h}\right). \tag{75}$$

A derivation of the complex-step approximation is given by Martins et al. [40]. Since only a forward step is taken in the imaginary direction, the complex-step method requires $3n$ runs compared to the $6n$ required by central difference. While the complex-step method can be

faster and more accurate than a finite-difference method, the number of required solution evaluations is prohibitive.

Another approach is automatic differentiation. Software packages can automatically produce code which runs alongside a program and calculates the gradients as the program executes. This approach has been successfully used in the development of discrete adjoint Navier–Stokes codes [41]. However, automatic differentiation implementations can suffer from memory inefficiencies. In addition, a bespoke differentiation approach where derivatives can be easily computed can outperform an automatic differentiation approach.

Many codes have been differentiated using the adjoint method. The adjoint method uses a linear algebra technique to obtain gradients of the solution alongside the solution. The adjoint method has been successfully applied to Navier–Stokes equations [42]. However, the computational methods used within HI-Mach are much simpler than a Navier–Stokes code. No large linear or non-linear systems are solved nor are any PDEs solved. The adjoint method is therefore not appropriate for differentiating HI-Mach. HI-Mach will be directly differentiated to obtain the sensitivities. The obtained geometric sensitivity can be converted to the sensitivity with respect to a design parameter with the use of a tool like Engineering Sketch Pad.

2.7.1. Definitions

HI-Mach runs unstructured meshes composed of triangular panels. These meshes are a discrete representation of a geometry. Mathematically, a mesh of a geometry is composed of n vertices, and it is described by the set of vertex coordinates

$$\chi = \begin{bmatrix} x_1 \\ \vdots \\ x_n \\ y_1 \\ \vdots \\ y_n \\ z_1 \\ \vdots \\ z_n \end{bmatrix} \tag{76}$$

which is an $3n \times 1$ column vector. Vertices within a geometry are connected together into m panels. The vertex position is described by the 3×1 column vector

$$\mathbf{p}_i = \begin{bmatrix} x_i \\ y_i \\ z_i \end{bmatrix} \tag{77}$$

The edge going from vertex i to vertex j is

$$\mathbf{e}_{ij} = \mathbf{p}_j - \mathbf{p}_i \tag{78}$$

which is also a 3×1 column vector. Definitions for dot and cross products are found in Appendix A.1.

2.7.2. Geometric Derivatives

The panel inclination relative to the freestream is given in Equation (1). Therefore, the derivative of a panel normal vector with respect to the mesh vertices is

$$\frac{\partial \theta}{\partial \chi} = -\frac{1}{\sqrt{1-(\hat{\boldsymbol{n}}\cdot\hat{\boldsymbol{v}}_\infty)^2}}\frac{\partial \hat{\boldsymbol{n}}}{\partial \chi}\cdot\hat{\boldsymbol{v}}_\infty \tag{79}$$

This is a $1 \times n$ row vector. Therefore, the complete set of derivatives of all of the panel inclinations with respect to all of the vertex locations is an $m \times n$ matrix.

The area of the panel made up of vertices $\boldsymbol{p}_i$, $\boldsymbol{p}_j$, and $\boldsymbol{p}_k$ is given by

$$A = \frac{|\boldsymbol{e}_{ij}\times\boldsymbol{e}_{jk}|}{2} = \frac{\sqrt{\left(\boldsymbol{e}_{ij}\times\boldsymbol{e}_{jk}\right)\cdot\left(\boldsymbol{e}_{ij}\times\boldsymbol{e}_{jk}\right)}}{2} \tag{80}$$

Therefore, the derivative of panel area with respect to the geometry is

$$\frac{\partial A}{\partial \chi} = \frac{1}{2\sqrt{\left(\boldsymbol{e}_{ij}\times\boldsymbol{e}_{jk}\right)\cdot\left(\boldsymbol{e}_{ij}\times\boldsymbol{e}_{jk}\right)}}\left(\frac{\partial}{\partial \chi}\left[\boldsymbol{e}_{ij}\times\boldsymbol{e}_{jk}\right]\right)\cdot\left(\boldsymbol{e}_{ij}\times\boldsymbol{e}_{jk}\right) \tag{81}$$

which is a $1 \times n$ row vector. The other geometric derivatives are found in Appendix A.2.

2.7.3. Inviscid Pressure Derivatives

The core of HI-Mach's aerodynamic methods is the inviscid pressure solution. As a review, the pressure on each panel is considered independent of the surrounding panels. In addition, the pressure is considered to be purely a function of the panel inclination, θ, with respect to the freestream. Panels on a geometry are classified as one of three types: windward, leeward, and base. The pressure on base panels is a constant, so it does not vary with panel inclination. Thus, the derivative of the pressure on base panels is 0. The pressure on windward and leeward panels varies with respect to panel inclination.

Four methods are presented in this paper to calculate the pressure in a windward region. The first two of these methods are the straight and modified Newtonian methods. The sensitivity of the straight and modified Newtonian methods, presented in Equation (4), with respect to the vertex coordinates is given as

$$\frac{\partial C_{P,\text{Newtonian}}}{\partial \chi} = 2C_{P,\max}\sin(\theta)\cos(\theta)\frac{\partial \theta}{\partial \chi} = C_{P,\max}\sin(2\theta)\frac{\partial \theta}{\partial \chi} \tag{82}$$

The third windward method is the tangent-cone method. For computational speed, it is implemented using a tabulated database of coefficients as shown in Equation (15). Thus, the derivative of the tangent cone panel pressure coefficient with respect to the vertex locations is trivially found to be

$$\frac{\partial C_{P,\text{TC}}}{\partial \chi} = \left(C_1 + 2C_2\theta + 3C_3\theta^2 + 4C_4\theta^3 + 5C_5\theta^4 + 6C_6\theta^5\right)\frac{\partial \theta}{\partial \chi} \tag{83}$$

The fourth windward method presented is the tangent-wedge method covered in Equations (6)–(10). The derivative of the tangent-wedge pressure coefficient with respect to the vertex coordinates is obtained using the chain rule

$$\frac{\partial C_{P,\text{TW}}}{\partial \chi} = \frac{2}{\gamma M_\infty^2 P_\infty}\frac{\partial P_2}{\partial \chi} = \frac{4}{\gamma+1}\sin(2\beta)\frac{\partial \beta}{\partial \chi} \tag{84}$$

The $\partial\beta/\partial\chi$ term has a lengthy expression and is contained in Appendix A.3.

The pressure coefficient on leeward surfaces is given by the Prandtl–Meyer relation, which determines the boundary layer edge Mach number on an expansion surface. The pressure is then derived from the Mach number using the isentropic relations. The panel pressure coefficient is given by Equation (19). The derivative of the pressure coefficient with respect to the geometry can be expanded using the chain rule

$$\frac{\partial C_{P,\mathrm{PM}}}{\partial \chi} = \frac{\partial C_{P,\mathrm{PM}}}{\partial M}\frac{\partial M}{\partial \theta}\frac{\partial \theta}{\partial \chi} \tag{85}$$

The intermediate derivatives are given in Appendix A.3.

2.7.4. Thermodynamic Property Derivatives

HI-Mach produces estimates of viscous drag and convective heating as described earlier. These estimates require the calculation of the gas thermodynamic properties on each panel. Derivatives of these properties with respect to the geometry are produced here. The pressure on a panel is given by Equation (22). The derivative with respect to the geometry is

$$\frac{\partial P_e}{\partial \chi} = \frac{P_\infty \gamma M_\infty^2}{2}\frac{\partial C_P}{\partial \chi} \tag{86}$$

where the second term has been determined previously. The pressure is assumed to be constant throughout the boundary layer. The boundary layer edge Mach number is given by Equation (24). The derivative with respect to the geometry is

$$\frac{\partial M_e}{\partial \chi} = \frac{\partial M_e}{\partial P_e}\frac{\partial P_e}{\partial \chi} = \frac{-P_0}{\gamma P_e^2\sqrt{\frac{2}{\gamma-1}\left(\left(\frac{P_0}{P_{e,i}}\right)^{\frac{\gamma-1}{\gamma}}-1\right)}}\left(\frac{P_e}{P_0}\right)^{\frac{1}{\gamma}}\frac{\partial P_e}{\partial \chi}. \tag{87}$$

The boundary layer edge temperature is defined by Equation (28). The derivative of the boundary layer edge temperature with respect to the geometry is

$$\frac{\partial T_e}{\partial \chi} = \frac{\partial T_e}{\partial M_e}\frac{\partial M_e}{\partial \chi} = \frac{-4T_0(\gamma-1)M_e}{(2+[\gamma-1]M_e^2)^2}\frac{\partial M_e}{\partial \chi} \tag{88}$$

The boundary layer edge density is also obtained through the ideal gas law. The derivative of the boundary layer edge density with respect to the geometry is

$$\frac{\partial \rho_e}{\partial \chi} = \frac{\partial \rho_e}{\partial P_e}\frac{\partial P_e}{\partial \chi} + \frac{\partial \rho_e}{\partial T_e}\frac{\partial T_e}{\partial \chi} = \frac{1}{RT_e}\frac{\partial P_e}{\partial \chi} - \frac{P_e}{RT_e^2}\frac{\partial T_e}{\partial \chi} \tag{89}$$

The dynamic viscosity is governed by Sutherland's law, which is reproduced in Equation (32). The derivative of the dynamic viscosity with respect to geometry is

$$\frac{\partial \mu}{\partial \chi} = \mu_{\mathrm{ref}}\left(\frac{3}{2}\sqrt{\frac{T}{T_{\mathrm{ref}}}}\frac{T_{\mathrm{ref}}+S}{T+S} - \left(\frac{T}{T_{\mathrm{ref}}}\right)^{\frac{3}{2}}\frac{T_{\mathrm{ref}}+S}{(T+S)^2}\right)\frac{\partial T}{\partial \chi} \tag{90}$$

where S, μ_{ref}, and T_{ref} are reference properties for a particular gas. In this instance, the boundary layer edge temperature T_e is replaced with a general temperature, T, since the viscosity at the wall is also often considered. In HI-Mach, the viscosity and Prandtl number can also be computed by referencing tabulated data with respect to temperature and pressure. The quantities are calculated by linear interpolation on the tabulated data, so the derivatives are trivially obtained by the slope of the interpolation.

2.7.5. Edge Velocity Derivatives

Two quantities used for computing boundary layer edge velocity are $\hat{\boldsymbol{e}}_{\text{stream}}$ and $\hat{\boldsymbol{e}}_{\text{perp}}$ These unit vectors are aligned and perpendicular with the velocity on the surface of the panel, respectively. Their definitions and derivatives are

$$\hat{\boldsymbol{e}}_{\text{stream}} = \frac{\boldsymbol{e}_{\text{stream}}}{|\boldsymbol{e}_{\text{stream}}|} = \frac{\left(\hat{\boldsymbol{n}} \times \hat{\boldsymbol{V}}_{\infty}\right) \times \hat{\boldsymbol{n}}}{\left|\left(\hat{\boldsymbol{n}} \times \hat{\boldsymbol{V}}_{\infty}\right) \times \hat{\boldsymbol{n}}\right|} \tag{91}$$

$$\frac{\partial \hat{\boldsymbol{e}}_{\text{stream}}}{\partial \chi} = \frac{\frac{\partial \boldsymbol{e}_{\text{stream}}}{\partial \chi}|\boldsymbol{e}_{\text{stream}}| - \boldsymbol{e}_{\text{stream}} \frac{\boldsymbol{e}_{\text{stream}} \cdot \frac{\partial \boldsymbol{e}_{\text{stream}}}{\partial \chi}}{|\boldsymbol{e}_{\text{stream}}|}}{|\boldsymbol{e}_{\text{stream}}|^2} \tag{92}$$

where

$$\frac{\partial \boldsymbol{e}_{\text{stream}}}{\partial \chi} = \left(\frac{\partial \hat{\boldsymbol{n}}}{\partial \chi} \times \hat{\boldsymbol{V}}_{\infty}\right) \times \hat{\boldsymbol{n}} + \left(\hat{\boldsymbol{n}} \times \hat{\boldsymbol{V}_{\infty}}\right) \times \frac{\partial \hat{\boldsymbol{n}}}{\partial \chi}. \tag{93}$$

The unit vector perpendicular to the panel and the local streamline direction is defined by

$$\hat{\boldsymbol{e}}_{\text{perp}} = \frac{\boldsymbol{e}_{\text{perp}}}{|\boldsymbol{e}_{\text{perp}}|} = \frac{\hat{\boldsymbol{n}} \times \hat{\boldsymbol{e}}_{\text{stream}}}{|\hat{\boldsymbol{n}} \times \hat{\boldsymbol{e}}_{\text{stream}}|} \tag{94}$$

Its derivative is computed similarly to the derivative of $\hat{\boldsymbol{e}}_{\text{stream}}$ as presented in Equation (92), except the quantity $\frac{\partial \boldsymbol{e}_{\text{perp}}}{\partial \chi}$ is given as

$$\frac{\partial \boldsymbol{e}_{\text{perp}}}{\partial \chi} = \frac{\partial \hat{\boldsymbol{n}}}{\partial \chi} \times \hat{\boldsymbol{e}}_{\text{stream}} + \hat{\boldsymbol{n}} \times \frac{\partial \hat{\boldsymbol{e}}_{\text{stream}}}{\partial \chi} \tag{95}$$

The magnitude of the boundary layer edge velocity V_e is given by Equation (30). The velocity is defined on a per-panel basis by

$$\boldsymbol{V}_e = \hat{\boldsymbol{e}}_{\text{stream}} V_e \tag{96}$$

The derivative of the boundary layer edge velocity vector on a panel with respect to the geometry is

$$\begin{aligned} \frac{\partial \boldsymbol{V}_e}{\partial \chi} &= \frac{\partial \boldsymbol{V}_e}{\partial M_e}\frac{\partial M_e}{\partial \chi} + \frac{\partial \boldsymbol{V}_e}{\partial T_e}\frac{\partial T_e}{\partial \chi} + \frac{\partial \boldsymbol{V}_e}{\partial \hat{\boldsymbol{e}}_{\text{stream}}}\frac{\partial \hat{\boldsymbol{e}}_{\text{stream}}}{\partial \chi} \\ &= \hat{\boldsymbol{e}}_{\text{stream}}\sqrt{\gamma \frac{R_U}{m_{\text{mol}}} T_e}\frac{\partial M_e}{\partial \chi} + \hat{\boldsymbol{e}}_{\text{stream}} M_e \frac{\gamma \frac{R_U}{m_{\text{mol}}}}{2\sqrt{\gamma \frac{R_U}{m_{\text{mol}}} T_e}}\frac{\partial T_e}{\partial \chi} + V_e \frac{\partial \hat{\boldsymbol{e}}_{\text{stream}}}{\partial \chi} \end{aligned} \tag{97}$$

where $\frac{R_U}{m_{\text{mol}}}$ is the specific gas constant of the gas in question given by.

2.7.6. Reference Temperature Derivatives

For viscous calculations in the acreage regions of the body, a reference temperature is used to evaluate the thermodynamic properties. The reference temperature can be expressed conveniently as

$$T^* = a_1 T_e + a_2 T_w + a_3 T_e M_e^2 \tag{98}$$

where the values of coefficients a_1, a_2, and a_3 are available for various reference temperature models shown in Equations (33)–(35). It is convenient to split up the derivative of the

reference temperature into two parts, one which depends on the derivative of the wall temperature, and one that does not, resulting in

$$\frac{\partial T^*}{\partial \chi} = \left.\frac{\partial T^*}{\partial \chi}\right|_{T_w} + \frac{\partial T^*}{\partial T_w}\frac{\partial T_w}{\partial \chi} \tag{99}$$

Note that $|_{T_w}$ implies $\partial T_w/\partial \chi = 0$. The respective terms of Equation (99) are given simply as

$$\left.\frac{\partial T^*}{\partial \chi}\right|_{\partial T_w/\partial \chi = 0} = a_1\frac{\partial T_e}{\partial \chi} + a_3\left(M_e^2\frac{\partial T_e}{\partial \chi} + 2M_eT_e\frac{\partial M_e}{\partial \chi}\right) \tag{100}$$

and

$$\frac{\partial T^*}{\partial T_w} = a_2 \tag{101}$$

2.7.7. Friction Coefficient Derivatives

The friction coefficient is used in calculating the viscous drag and acreage heating. The friction coefficient can be generally expressed as

$$c_f = k_{c_f}\mathrm{Re}^{-m_{cf}} \tag{102}$$

where the values of k_{c_f} and $\mathrm{Re}^{-m_{cf}}$ differ depending on which correlation is used for the friction coefficient and are shown in Equations (36)–(38). Similarly to how the derivative of the reference temperature is split in Equation (99), the derivative of the friction coefficient is obtained in two parts. The first neglects changes in wall temperature. The two resulting expressions are

$$\left.\frac{\partial c_f}{\partial \chi}\right|_{T_w} = c_f m_{cf}\left[\mu^{*^{-1}}\left.\frac{\partial \mu^*}{\partial \chi}\right|_{T_w} - \rho^{*^{-1}}\left.\frac{\partial \rho^*}{\partial \chi}\right|_{T_w} - V_e^{-1}\frac{\partial V_e}{\partial \chi} - x^{-1}\frac{\partial x}{\partial \chi}\right] \tag{103}$$

$$\frac{\partial c_f}{\partial T_w} = c_f m_{cf}\left[\mu^{*^{-1}}\frac{\partial \mu^*}{\partial T^*}\frac{\partial T^*}{\partial T_w} - \rho^{*^{-1}}\frac{\partial \rho^*}{\partial T^*}\frac{\partial T^*}{\partial T_w}\right] \tag{104}$$

2.7.8. Stagnation Heating Derivatives

The heating to a stagnation region is given by Equation (57). Like the reference temperature and friction coefficient, the derivative of stagnation heating is split into two parts. The derivative neglecting the wall temperature changes is

$$\begin{aligned}\left.\frac{\partial \dot{q}_s}{\partial \chi}\right|_{T_w} = \dot{q}_s\Bigg[&0.43\rho_e^{-1}\frac{\partial \rho_e}{\partial \chi} + 0.43\mu_e^{-1}\frac{\partial \mu_e}{\partial \chi} + 0.5\left(\frac{du_e}{dx}\right)^{-1}\frac{\partial \frac{du_e}{dx}}{\partial \chi}\\ &+ 0.07\rho_w^{-1}\frac{\partial \rho_w}{\partial p}\frac{\partial p}{\partial \chi} + 0.07\mu_w^{-1}\frac{\partial \mu_w}{\partial p}\frac{\partial p}{\partial \chi} - 0.6\mathrm{Pr}_w^{-1}\frac{\partial \mathrm{Pr}_w}{\partial p}\frac{\partial p}{\partial \chi}\Bigg]\end{aligned} \tag{105}$$

The derivative with respect to wall temperature is similarly obtained by

$$\frac{\partial \dot{q}_s}{\partial T_w} = \dot{q}_s\left[-(h_{aw}-h_w)^{-1}\frac{\partial h_w}{\partial T_w} + 0.07\rho_w^{-1}\frac{\partial \rho_w}{\partial T_w} + 0.07\mu_w^{-1}\frac{\partial \mu_w}{\partial T_w} - 0.6\mathrm{Pr}_w^{-1}\frac{\partial \mathrm{Pr}_w}{\partial T_w}\right] \tag{106}$$

The derivative of the boundary layer edge velocity gradient is the most difficult to compute of all these terms and is given in Appendix A.4. The geometric constant is given as

$$k_{\text{geom}} = 0.767\sqrt{\frac{1 + |\frac{\kappa_{\text{attach}}}{\kappa_{\text{perp}}}|}{2}} \tag{107}$$

where the ratio $\kappa_{\text{attach}}/\kappa_{\text{perp}}$ always takes on a value between -1 and 1. The derivative is then

$$\frac{\partial k_{\text{geom}}}{\partial \chi} = \frac{0.767}{2\sqrt{2}\sqrt{1 + |\frac{\kappa_{\text{attach}}}{\kappa_{\text{perp}}}|}} \text{sgn}\left(\frac{\kappa_{\text{attach}}}{\kappa_{\text{perp}}}\right) \frac{\frac{\partial \kappa_{\text{attach}}}{\partial \chi}\kappa_{\text{perp}} - \kappa_{\text{attach}}\frac{\partial \kappa_{\text{perp}}}{\partial \chi}}{\kappa_{\text{perp}}^2} \tag{108}$$

Swept attachment lines result in lower heating rates. In HI-Mach, the correction for sweep is only applied to cylindrical stagnation regions, which are defined as a region where $|\kappa_{\text{attach}}/\kappa_{\text{perp}}| > 3$. The sweep angle is calculated as

$$\Lambda = |\arccos(|\hat{\boldsymbol{a}}_L \cdot \boldsymbol{v}_\infty|) - \frac{\pi}{2}| \tag{109}$$

where the attachment line direction $\hat{\boldsymbol{a}}_L$ and the freestream direction $\boldsymbol{v}_\infty$ are assumed to be unit-length. The effects of sweep are included in the heat rate by the multiplication of a sweep factor, resulting in

$$k_{\text{sweep}} = \cos^{1.1}\Lambda + 0.05\sin^2\Lambda \tag{110}$$

The derivatives of these quantities are then

$$\frac{\partial \Lambda}{\partial \chi} = \frac{\text{sgn}(\hat{\boldsymbol{a}}_L \cdot \hat{\boldsymbol{v}}_\infty)}{\sqrt{1 - (\hat{\boldsymbol{a}}_L \cdot \hat{\boldsymbol{v}}_\infty)^2}}\left(\frac{\partial \hat{\boldsymbol{a}}_L}{\partial \chi} \cdot \hat{\boldsymbol{v}}_\infty\right) \tag{111}$$

$$\frac{\partial k_{\text{sweep}}}{\partial \chi} = \frac{\partial \Lambda}{\partial \chi}\sin\Lambda\cos\Lambda\left(0.1 - 1.1(\cos\Lambda)^{-0.9}\right) \tag{112}$$

If the effects of sweep are considered, the derivative of stagnation heating in Equations (105) and (106) is multiplied by k_{sweep}, and an additional term must be added to the derivative of the stagnation heating to account for sweep effects.

2.7.9. Acreage Heating Derivatives

The heating to the acreage region is given by

$$\dot{q}_a = \frac{c_f^*}{2}\rho^* V_e(h_{aw} - h_w)\text{Pr}^{*-2/3} \tag{113}$$

which takes advantage of the simplified formulation for c_f^* in Equation (102). The derivative, split into two parts, is

$$\begin{aligned}\left.\frac{\partial \dot{q}_a}{\partial \chi}\right|_{T_w} = \dot{q}_a\Bigg[&c_f^{*-1}\left.\frac{\partial c_f^*}{\partial \chi}\right|_{T_w} + \rho^{*-1}\left.\frac{\partial \rho^*}{\partial \chi}\right|_{T_w} + (h_{aw} - h_w)^{-1}\left.\frac{\partial h_{aw}}{\partial \chi}\right|_{T_w} \\ &+ V_e^{-1}\frac{\partial V_e}{\partial \chi} - \frac{2}{3}\text{Pr}^{*-1}\left.\frac{\partial \text{Pr}^*}{\partial \chi}\right|_{T_w}\Bigg]\end{aligned} \tag{114}$$

and

$$\frac{\partial \dot{q}_a}{\partial T_w} = \dot{q}_a\left[c_f^{*-1}\frac{\partial c_f^*}{\partial T_w} + \rho^{*-1}\frac{\partial \rho^*}{\partial T_w} - (h_{aw} - h_w)^{-1}\frac{\partial h_w}{\partial T_w} - \frac{2}{3}\text{Pr}^{*-1}\frac{\partial \text{Pr}^*}{\partial T_w}\right] \tag{115}$$

2.7.10. Radiation Equilibrium Derivatives

The wall conditions currently implemented in HI-Mach are the fixed wall temperature and radiation equilibrium wall. For the fixed wall temperature, the term $\partial T_w/\partial \chi$ is 0. For a radiation wall equilibrium, the wall temperature is a function of the geometry. The governing equation, reproduced from Equation (44) of [2], is

$$\epsilon_w \sigma T_w^4 = \dot{q}_w \tag{116}$$

Differentiating this with respect to the geometry yields

$$\frac{\partial \dot{q}_w}{\partial \chi} = 4\epsilon_w \sigma T_w^3 \frac{\partial T_w}{\partial \chi} \tag{117}$$

The derivative of the heat flux to the wall can be expressed as

$$\frac{\partial \dot{q}_w}{\partial \chi} = \left.\frac{\partial \dot{q}_w}{\partial \chi}\right|_{T_w} + \frac{\partial \dot{q}_w}{\partial T_w}\frac{\partial T_w}{\partial \chi} \tag{118}$$

Equations (117) and (118) can be equated to yield

$$\frac{\left.\frac{\partial \dot{q}_w}{\partial \chi}\right|_{T_w}}{4\epsilon_w \sigma T_w^3 - \frac{\partial \dot{q}_w}{\partial T_w}} = \frac{\partial T_w}{\partial \chi} \tag{119}$$

which gives a direct solution for $\partial T_w/\partial \chi$. For a stagnation panel, the quantity $\partial \dot{q}_w/\partial T_w$ is given by Equation (106), and for an acreage panel, it is given by Equation (115).

2.7.11. Curvature Derivatives

Calculating the curvature is a complicated multistep process. The process is fully described in [2]. It involves transforming vectors into a local coordinate system, solving least squares problems on each vertex, then rotating and averaging tensors based on corner angles, solving a rank-2 eigenvalue problem, and then transforming $\mathbb{R}^2$ vectors back into $\mathbb{R}^3$. Each of these steps is a function of vertex position and requires intermediate derivatives. Instead of attempting to directly take sensitivities of the curvature process, central differencing is used to compute the derivatives of the curvature.

The curvature on a panel is a function of the normal vectors of the three vertices which make up the panel. The normal vector of a given vertex is a function of all vertices adjacent to that vertex. Therefore, the curvature on a panel is a function of the three vertices which define the panel as well as any adjacent vertices. To compute the derivatives of curvature, each of these vertices must be perturbed in 3 directions, and the curvature problem must be solved. This can be expensive, depending on the mesh connectivity.

Thankfully, these derivatives are only necessary on attachment panels. For most geometries, the number of acreage panels vastly outweighs the number of stagnation panels. Table 2 shows the proportion of attachment panels on a variety of geometries.

More complex geometries with wings, fins, and chines have a higher proportion of attachment panels. Simple blunt-nosed geometries have very low proportions of attachment panels. In general, the more complex the flow pattern across a geometry, the greater the number of attachment panels. Nonetheless, even the most complex geometries have less than 5% attachment panels. As a result, it is not prohibitively expensive to compute the derivatives of curvature using central differencing.

Table 2. Proportion of attachment line panels across various geometries.

Geometry Name	Description	Attachment Panel Count	Total Panel Count	Proportion of Attachment Panels (%)
HL-20	Winged lifting re-entry vehicle	711	13,546	5.25
GHV	Streamlined low hypersonic aircraft	2096	44,624	4.70
HB-2	Blunt nosed, tri-conic flared cone	5	13,629	0.037
Sphere-Cone	Blunt nosed, single cone angle	4	58,924	0.0068

HI-Mach implements two methods for mesh curvature calculations, which are described in detail in [2]. The difference-of-normals method only uses 1-ring vertices, while the paraboloid method uses 3-ring vertices. As a result, the curvature when computed with the paraboloid method depends on many more vertices. Therefore, computing derivatives via central differencing for the the difference-of-normals method is much cheaper than the paraboloid method, since fewer perturbations must be performed.

2.7.12. Running Length Derivatives

The running length is the distance a streamline travels from a stagnation point to a certain point on the vehicle. The running length is used to compute the surface Reynolds number, which is in turn used to compute the convective heat flux to the surface. The running length on panel i is computed by

$$x_i = \sum_{j}^{N} x_j \tag{120}$$

where the sum traverses all the panels from the stagnation point to panel i. In other words, the running length on a certain panel is the sum of discrete running lengths on the preceding panels. The contribution to overall running length from panel j is

$$x_j = |\hat{x}_j - \hat{x}_{j-1}| \tag{121}$$

where $\hat{x}_j$ and $\hat{x}_{j-1}$ are the points where the streamline leaves panels j and $j-1$, respectively. The method for calculating running length is described in detail in [1]. The sensitivity of the total running length is

$$\frac{\partial x}{\partial \chi} = \sum_{i}^{N} \frac{\partial x_i}{\partial \chi} \tag{122}$$

where the sensitivity of each individual running length is given as

$$\frac{\partial x_i}{\partial \chi} = \frac{(\hat{x}_i - \hat{x}_{i-1}) \cdot \left(\frac{\partial \hat{x}_i}{\partial \chi} - \frac{\partial \hat{x}_{i-1}}{\partial \chi} \right)}{|\hat{x}_i - \hat{x}_{i-1}|}. \tag{123}$$

where the derivatives of streamline end points are given in Appendix A.5.

2.7.13. Velocity Derivatives

For each panel on the surface, a linear velocity distribution is defined to allow for the tracing of streamlines and attachment line detection. The derivative of the coefficients in Equation (44) is given by

$$\frac{\partial \{J\}}{\partial \chi} = \frac{\partial [Q]}{\partial \chi} \{S\} + [Q] \frac{\partial \{S\}}{\partial \chi} \tag{124}$$

where

$$\{J_u\} = \begin{Bmatrix} a_1 \\ b_1 \\ c_1 \end{Bmatrix} \tag{125}$$

$$\{J_v\} = \begin{Bmatrix} a_2 \\ b_2 \\ c_2 \end{Bmatrix} \tag{126}$$

The derivatives in Equation (124) are given in Appendix A.6.

2.7.14. Attachment Line Derivatives

Attachment lines are used to identify where streamlines start on the body and where stagnation heating is applied as opposed to acreage heating. The first attachment line detection method is by an eigenvalue analysis of the linear velocity field. As described in [1], the panel vertices are transformed into a coordinate system where the eigenvectors are orthogonal. If the panel intersects the X-axis, the panel contains an attachment line and the attachment line direction is the eigenvector. The derivative of the attachment line direction is then given by Equation (A33).

The second attachment line detection method is through streamline tracing. As described in [1], if a streamline leaves and immediately returns to a panel, the panel is classified as an attachment panel. The attachment line direction is coincident with the edge across which the streamline 'bounces' back and forth. Therefore, the derivative of the attachment line direction is the derivative of the edge unit vector, which is derived in Equation (A7).

2.7.15. Aerodynamic Force Derivatives

The total force coefficient is a 3×1 column vector which includes the total force coefficient in x, y, and z, normalized against a reference area, which is given as

$$\boldsymbol{C}_F = \sum_{i=1}^{m} \frac{A_i}{A_{\text{ref}}} \left(\hat{\boldsymbol{v}}_A \tau_{w,i} - \hat{\mathbf{n}}_i C_{p,i} \right) \tag{127}$$

The first part of Equation (127) is the viscous component, and the second part is the inviscid component. The derivative of the total force coefficient with respect to the geometry is given as

$$\frac{\partial \boldsymbol{C}_F}{\partial \chi} = \frac{1}{A_{\text{ref}}} \sum_{i=1}^{m} \left[\frac{\partial A_i}{\partial \chi} \left(\hat{\boldsymbol{v}}_A \tau_{w,i} - \hat{\mathbf{n}}_i C_{p,i} \right) + A_i \left(\frac{\partial \hat{\boldsymbol{v}}_A}{\partial \chi} \tau_{w,i} + \hat{\boldsymbol{v}}_A \frac{\partial \tau_{w,i}}{\partial \chi} - \frac{\partial \hat{\mathbf{n}}_i}{\partial \chi} C_{p,i} - \hat{\mathbf{n}}_i \frac{\partial C_{p,i}}{\partial \chi} \right) \right] \tag{128}$$

The lift and drag coefficients are often desired as the final result of an aerodynamic analysis. They can be obtained from the total force coefficient with

$$C_L = \boldsymbol{C}_F \cdot \hat{\boldsymbol{n}}_{\text{lift}}, \quad C_D = \boldsymbol{C}_F \cdot \hat{\boldsymbol{v}}_\infty \tag{129}$$

where $\hat{\boldsymbol{n}}_{\text{lift}} = \hat{\boldsymbol{n}}_{\text{pitch}} \times \hat{\boldsymbol{n}}_{\text{nose}}$ and $\hat{\boldsymbol{n}}_{\text{pitch}}$ points out the right wing of the aircraft and $\hat{\boldsymbol{n}}_{\text{nose}}$ points out the nose. The derivatives of these with respect to the geometry are then

$$\frac{\partial C_L}{\partial \chi} = \frac{\partial \boldsymbol{C}_F}{\partial \chi} \cdot \hat{\boldsymbol{n}}_{\text{lift}}, \quad \frac{\partial C_D}{\partial \chi} = \frac{\partial \boldsymbol{C}_F}{\partial \chi} \cdot \hat{\boldsymbol{v}}_\infty \tag{130}$$

The pitching moment is given as

$$\boldsymbol{C}_M = \sum_{i=1}^{m} \frac{A_i}{A_{\text{ref}}\, l_{\text{ref}}} (\boldsymbol{x}_{\text{centroid}} - \boldsymbol{x}_{CG}) \times \left(\hat{\boldsymbol{v}}_A \tau_{w,i} - \hat{\mathbf{n}}_i C_{p,i}\right) \tag{131}$$

The derivative of the pitching moment is obtained as

$$\begin{aligned} \frac{\partial \boldsymbol{C}_M}{\partial \chi} = \frac{1}{A_{\text{ref}}\, l_{\text{ref}}} \sum_{i=1}^{m} \Bigg\{ & \frac{\partial A_i}{\partial \chi} [\boldsymbol{x}_{\text{centroid}} - \boldsymbol{x}_{CG}] \times \left[\hat{\boldsymbol{v}}_A \tau_{w,i} - \hat{\mathbf{n}}_i C_{p,i}\right] \\ & + A_i \left[\frac{\partial \boldsymbol{x}_{\text{centroid}}}{\partial \chi} \times \left(\hat{\boldsymbol{v}}_A \tau_{w,i} - \hat{\mathbf{n}}_i C_{p,i}\right) + (\boldsymbol{x}_{\text{centroid}} - \boldsymbol{x}_{CG}) \times \frac{\partial \left(\hat{\boldsymbol{v}}_A \tau_{w,i} - \hat{\mathbf{n}}_i C_{p,i}\right)}{\partial \chi} \right] \Bigg\} \end{aligned} \tag{132}$$

2.8. Assumptions and Limitations

The methods presented here benefit from a number of assumptions. These assumptions, which aid to simplify calculations, have certain inherit limitations. This section presents key assumptions associated with each method to inform the reader as to the applicability of present methods.

2.8.1. Inclination Methods

The local inclination methods are a simplified model for calculating pressure coefficients. They assume that the local pressure is independent of the rest of the geometry. In general, these methods will not be accurate where shock effects and interaction are to be expected. The Newtonian methods are expected to perform better the higher the Mach number. Good performance of the Newtonian methods at low Mach numbers ($M_\infty < 3$) is considered to be fortuitous. The tangent wedge/cone methods are not as dependent on Mach number. However, they assume that the geometry is akin to a wedge/cone.

2.8.2. Surface Properties

Many assumptions are made to fix the thermodynamic properties on the surface of the body. The first is the assumption of the surface flow passing through a normal shock. In reality, not all the flow on the surface passes through a normal shock. This is considered, however, to be a worst-case scenario. The normal shock assumption will result in higher heating rates and skin friction values than if the true shock angle was used. The second assumption is isentropic flow post shock. The isentropic assumption limits the flow to small perturbations and is assumed to perform better for a waverider than for a reentry vehicle. The last assumption is that of an ideal gas. The ideal gas assumption neglects high-temperature effects such as dissociation and variation in γ. For temperatures above about 800 K, the ideal gas assumption breaks down [4]. In regions of high-temperature flows, the ideal gas assumption will cause an overprediction in temperature.

2.8.3. Boundary Layer

Assuming a thin boundary layer neglects important viscous effects in hypersonics [43]. First, at the leading edge the formation of the boundary layer creates a larger displacement for the inviscid flow to move through, which creates a stronger shock. Second, extremely high temperatures in the boundary layer cause a decrease in density, ρ. To maintain mass flow, the boundary layer expands. Both of these effects are neglected when assuming thin boundary layers [4,43]. However, the computational cost of solving the full Navier–Stokes equation to deal with large boundary layers is prohibitive. For a low-fidelity code, the thin boundary layer assumption makes solving aerothermal problems tractable. Semi-empirical factors for reference temperature and enthalpy can help to offset the impact of neglected viscous effects.

A related assumption is that of a zero normal pressure gradient in a boundary layer. When boundary layers are thick or the entropy layer is swallowed by the boundary layer, the wall pressure is different from the edge pressure [4]. Making this assumption tends to underpredict skin friction and heat transfer [44]. However, in this low-fidelity paper, we assume zero normal pressure gradient to make the problem computationally tractable. Both the thin boundary layer and zero pressure gradient assumptions become less appropriate with faster flows [43,44].

2.8.4. Stagnation Heating

Assuming Le $= 1$ neglects chemically reacting flow effects and molecular wall recombination effects, both of which are important at reentry Mach numbers. In effect, the assumption neglects differences in diffusion properties for each chemical species [45]. This assumption tends to underpredict stagnation point heat transfer. The assumption is further complicated when considering wall chemistry effects. Wall catalycity has a non-negligible impact on heating and can void the assumption of Le $= 1$. The assumption that Le $= 1$ is commonly used in preliminary design work. As such, care must be taken as the design matures to confirm heating results which assume Le $= 1$ with more precise methods.

3. Results

The results presented in this paper consist of a study of the HL-20 lifting body reentry vehicle. This vehicle was chosen due to the availability of the geometry and associated wind tunnel data. Additional canonical geometries are included for further verification.

3.1. Aerodynamics

3.1.1. Convergence

In this section, the grid convergence of the inviscid methods is examined. The axial force coefficient on a hemisphere using the Modified Newtonian method is given by

$$C_x = \frac{C_{p,\max}}{2} \tag{133}$$

A grid convergence study was conducted on hemispheres of varying mesh resolutions to evaluate order of convergence. The results of the study are shown in Figure 9. The calculated order of convergence is 0.976.

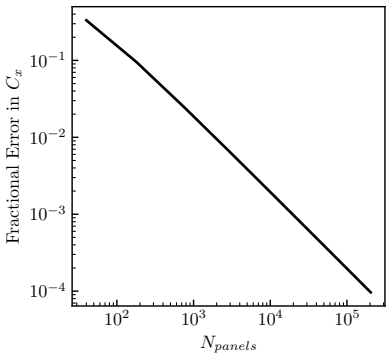


Figure 9. Fractional error in the axial force coefficient of hemisphere.

Using the tangent cone method, the axial force coefficient of a cone of radius 1 and cone angle θ_c with a surface pressure coefficient of C_p, is given by

$$C_x = C_p \sin\theta_c \sqrt{1 + \frac{1}{\tan\theta_c{}^2}} \tag{134}$$

A grid convergence study was run on the tangent cone method to evaluate the order of convergence and correct implementation. The results of the grid convergence study are plotted in Figure 10. The calculated order of convergence is 0.982, confirming that this method is first-order convergent. The reader should note that the error is calculated against the HI-Mach polynomial interpolated value, as discussed above.

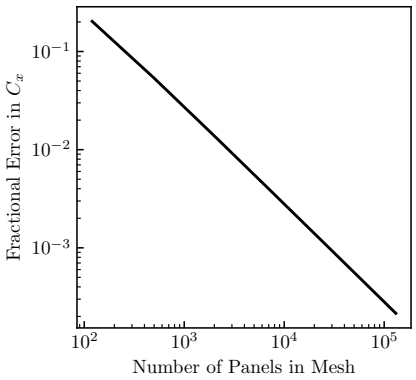


Figure 10. Fractional error in the axial force coefficient of cone.

3.1.2. Tangent Ogive

The accuracy of local panel inclination methods when applied to arbitrary bodies is dependent on the method chosen to evaluate the pressure coefficient on the windward side. Figure 11 displays the pressure coefficient on a tangent ogive, a cone-like geometry, at Mach 6.3 using each windward method discussed in a previous section. These pressure coefficients are compared against analytical shock expansion solutions in addition to experimental results. The tangent wedge method was the least accurate in predicting the pressure coefficient, which is perhaps because it is derived from two-dimensional oblique shock relations. The tangent cone method, which was derived from the Taylor–Maccoll equations for axisymmetric cones, performs the best of all the methods in predicting the pressure coefficient with a maximum error of 0.0066 compared to experimental results.

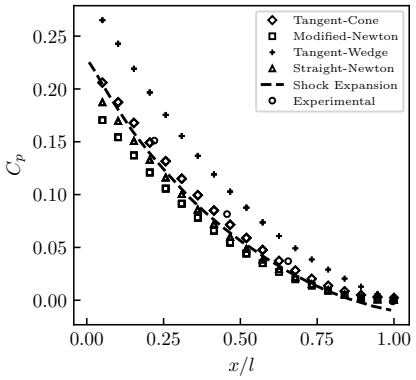


Figure 11. Tangent Ogive at Mach 6.3. Experimental and shock expansion results from Eggers et al. [46].

3.1.3. Double Wedge Wing

Figure 12 displays the pressure coefficient on the surface of a double wedge wing with a half wedge angle of 5°. HI-Mach results were compared to analytic shock expansion calculations for Mach numbers from 2.0 to 10.0 for angles of attack from 0° to 10°. HI-Mach was run using the tangent wedge method for windward surfaces and the Prandtl–Meyer method for leeward surfaces. The maximum error in the pressure coefficient between HI-Mach and shock expansion calculations was 0.0033.

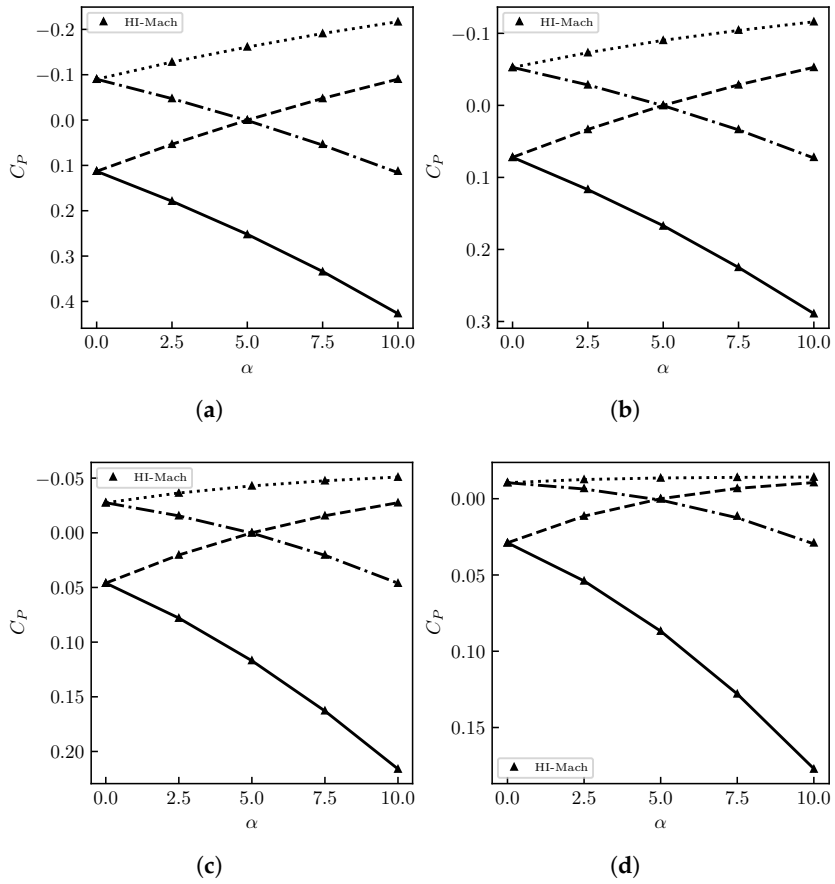


Figure 12. Surface pressure coefficients on 5° half-angle double-wedge airfoil predicted by HI-Mach calculations (discrete points) and shock-expansion theory (lines) for varying α in degrees. The line style indicates which surface the pressure coefficient is over. Solid: lower fore. Dashed: upper fore. Dash–dot: lower-aft. Dotted: upper-aft. (**a**) $M_\infty = 2.0$; (**b**) $M_\infty = 3.0$; (**c**) $M_\infty = 5.0$; (**d**) $M_\infty = 10.0$.

3.1.4. HL-20

Aerodynamic characteristics obtained by HI-Mach for the HL-20 were compared to wind tunnel tests by Ware [17]. Wind tunnel tests were performed by Ware [17] at a constant body length Reynolds number $Re = 3.4 \times 10^6$. With the HL-20 being a blunt geometry, the modified Newtonian method was used on the windward side. HI-Mach was run with and without viscous skin friction approximations at the same Reynolds number as the wind tunnel tests. The boundary layer was allowed to transition to turbulent. No grid convergence study is provided for the HL-20 due to the lack of availability of varying mesh densities.

Figure 13 shows results at Mach 4.5. This Mach number is close to the range that the modified Newtonian method is generally accepted as accurate (see Anderson [4]). In general, it appears that the inviscid HI-Mach solution slightly underpredicts both lift and drag. The viscous approximation brings the drag coefficient up closer to the experimental results at small angles of attack. The viscous approximation does not have any impact on the pitching moment coefficient. The maximum error between HI-Mach and the experimental results at Mach 4.5 was 11.9% for the lift coefficient and 9.2% for the drag coefficient. Figure 14 shows the results for Mach 1.6, which is much lower than the range where the modified Newtonian method is considered to be accurate. However, results from HI-Mach followed the experimental results well with a general underprediction of both lift and drag. The maximum error at Mach 1.6 was 21.5% for the lift coefficient and 16.3% for the drag coefficient.

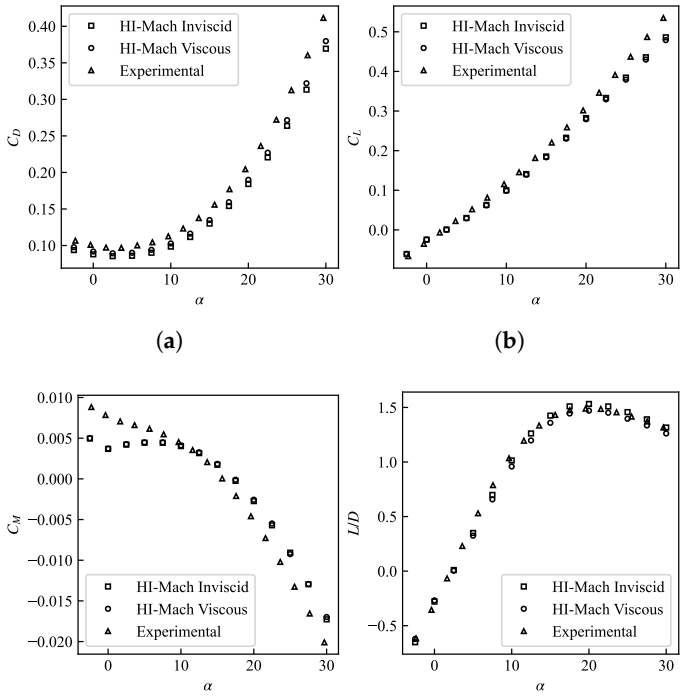


Figure 13. Aerodynamic Characteristics of HL-20 at Mach 4.5 for varying α in degrees. (**a**) Drag Coefficient; (**b**) Lift Coefficient; (**c**) Pitching Moment Coefficient; (**d**) Lift to Drag Ratio. Experimental and HI-Mach viscous results are at $\boldsymbol{Re} = 3.4 \times 10^6$. Reprinted with permission from Goates et al. [1]. Copyright ©2025 Goates.

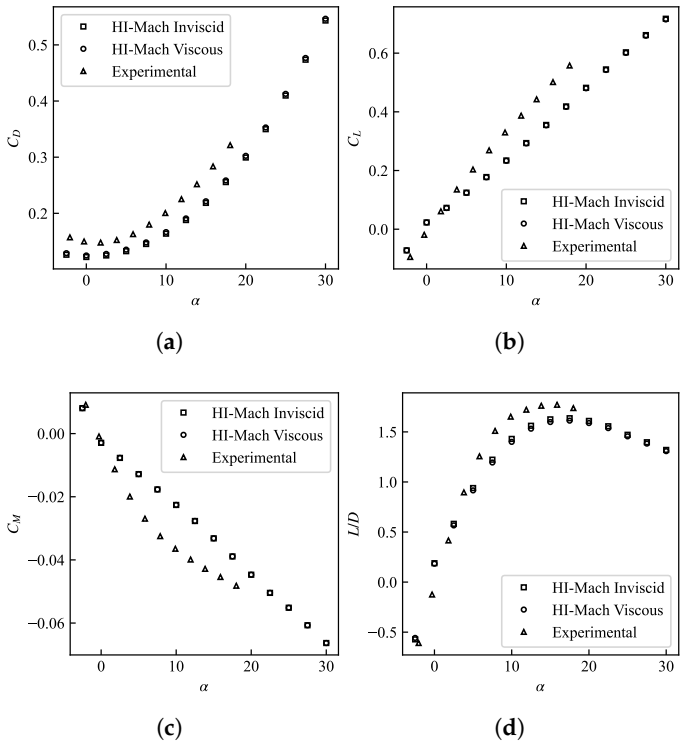


Figure 14. Aerodynamic characteristics of HL-20 at Mach 1.6 for varying α in degrees. (**a**) Drag Coefficient; (**b**) Lift Coefficient; (**c**) Pitching Moment Coefficient; (**d**) Lift to Drag Ratio. Experimental and HI-Mach viscous results are at $\boldsymbol{Re} = 3.4 \times 10^6$. Reprinted with permission from Goates et al. [1]. Copyright ©2025 Goates.

3.2. Heating

HI-Mach has been used to generate heating results. These results are compared to experimental results and numerical results from other codes. The results offer insights on the strengths and weaknesses of HI-Mach as well as areas for further improvement.

3.2.1. Sphere–Cone

Lee and Wurster produced CFD results for a sphere–cone with the NASA LAURA CFD code [47]. The cone angle is 15° and the length is 30 in. The spherical nose radius is 1.0 in for cases 1–6 and 1.1 in for case 7. Results from HI-Mach are compared to the CFD results. The CFD results and the HI-Mach results are both laminar. A grid convergence study was performed on the geometry at various grid resolutions. A grid with 35,000 triangles was sufficiently converged and used in HI-Mach to produce these results. HI-Mach was run with a calorically perfect gas model, Sutherland viscosities, and modified Newtonian pressures. Table 3 summarizes the freestream conditions for the comparison cases.

Table 3. Summary of tested cases for sphere–cone geometry.

	α (°)	M_∞	P_∞ (Pa)	ρ_∞ (kg/m^3)	Wall Condition
Case 1	20	11	103.48	1.33×10^{-3}	Radiative Equilibrium, $\epsilon = 0.89$
Case 2	20	11	50.57	6.66×10^{-4}	Radiative Equilibrium, $\epsilon = 0.89$
Case 3	20	13.16	50.57	6.66×10^{-4}	Radiative Equilibrium, $\epsilon = 0.89$
Case 4	20	13.16	40.69	5.45×10^{-4}	Radiative Equilibrium, $\epsilon = 0.89$
Case 5	20	16	11.48	1.71×10^{-4}	Radiative Equilibrium, $\epsilon = 0.89$
Case 6	20	18	11.48	1.71×10^{-4}	Radiative Equilibrium, $\epsilon = 0.89$
Case 7	0	10.6	198.09	1.46×10^{-2}	Cold Wall, $T_w = 300$ K

Results from the first two cases at $M_\infty = 11$ are presented in Figure 15. In Case 1 and Case 2, HI-Mach underpredicts heating at the stagnation point and along the windward centerline. HI-Mach likely underpredicts stagnation point heating because it models a calorically perfect gas and does not consider reactive catalytic effects. For these cases, LAURA used a fully catalytic wall. In addition, the increase in heating at $X/L \approx 0.1$ is due to the recompression effects caused by the bow shock. HI-Mach is only a surface code and does not model any shock interactions, so it is unable to capture this recompression. This discrepancy propagates aftward along the body and is visible in the near-constant offset between LAURA and HI-Mach in these results.

Results from Cases 3 and 4 at $M_\infty = 13.16$ are presented in Figure 16 In Cases 3 and 4, HI-Mach agrees much better with the LAURA results. For the same reason as in Cases 1 and 2, HI-Mach underpredicts stagnation point heating. However, the acreage heating prediction is better. This could be due to a smaller shock standoff distance at the higher freestream Mach number, diminishing the increase in recompression effects. HI-Mach slightly overpredicts the convective heating in the acreage region as compared to LAURA.

The results from Cases 5 and 6 at $M_\infty = 16$ and $M_\infty = 18$ are presented in Figure 17. In Case 5, HI-Mach accurately predicts stagnation heating. For Case 6, HI-Mach underpredicts peak stagnation heating. In both of these cases, HI-Mach underpredicts centerline acreage heating. Visually, the underprediction appears to be a constant offset. Shock-surface interactions could be the cause of this constant heating offset. In addition, at high freestream Mach numbers, the assumptions that air is calorically perfect and non-reacting become worse. Therefore, HI-Mach can be expected to perform worse at high Mach numbers.

For the seventh case, both CFD and wind tunnel data are available. Information on how the wind tunnel measurements were obtained is available in [48]. The CFD and wind tunnel results are plotted against the HI-Mach results in Figure 18.

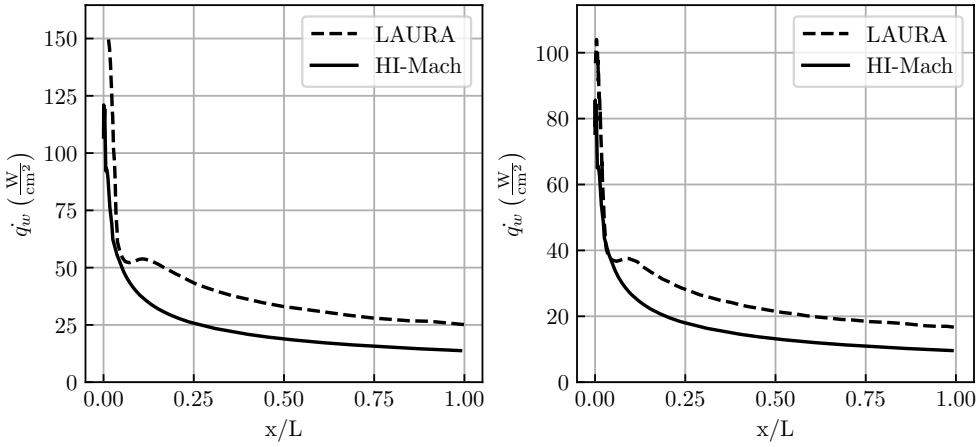


Figure 15. Comparison between HI-Mach and LAURA results for sphere-cone geometry at $M_\infty = 11$. (**a**) Case 1; (**b**) Case 2.

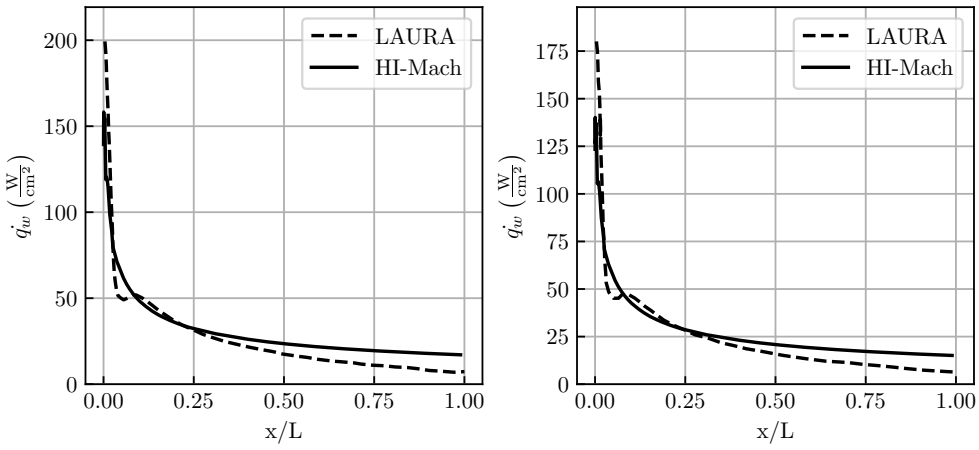


Figure 16. Comparison between HI-Mach and LAURA results for sphere–cone geometry at $M_\infty = 11$. (**a**) Case 3; (**b**) Case 4.

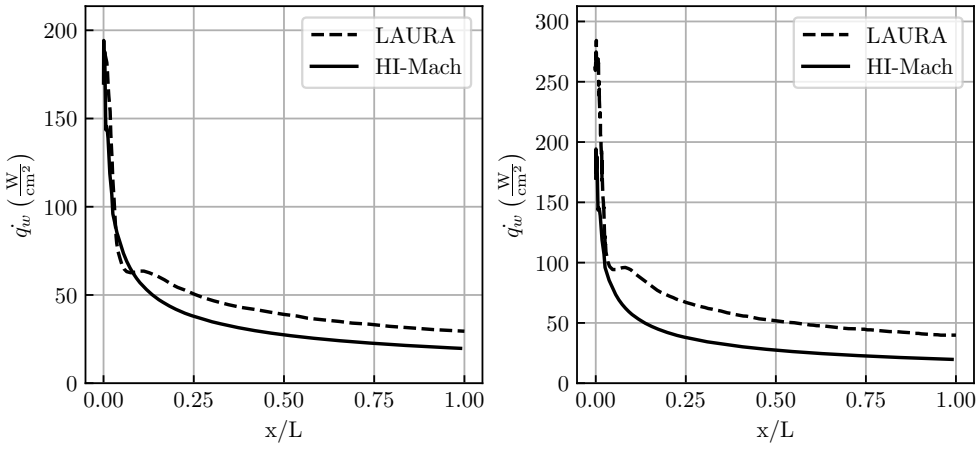


Figure 17. Comparison between HI-Mach and LAURA results for sphere–cone geometry at $M_\infty = 16$ and $M_\infty = 18$. (**a**) Case 5; (**b**) Case 6.

At these flow conditions, HI-Mach matches very well with the CFD results and wind tunnel data. This case is at zero angle of attack with a much higher freestream dynamic pressure. At zero angle of attack, shock reattachment and recompression effects are less important compared to the other cases. In addition, this case was run with a cold-wall model, which is different from the radiation equilibrium for the other cases. The implementation of radiation equilibrium in HI-Mach may be different than the implementation Lee and Wurster used for their LAURA results. This would explain some of the discrepancies in Cases 1–6.

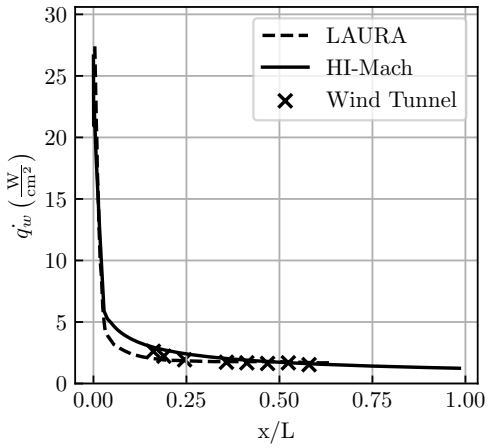


Figure 18. Comparison between HI-Mach, LAURA, and wind tunnel results for sphere–cone geometry.

3.2.2. HL-20

Horvath et al. conducted wind-tunnel measurements of surface heating rates on the HL-20 in a Mach 6 and a Mach 10 wind tunnel [49]. These experimental results are compared to HI-MACH using a laminar boundary layer, the Modified Newtonian pressure correlation, and tabulated viscosity data. The results from Horvath et al. [49] are given in terms of C_h/C_{h0}, which is the measured heat transfer coefficient divided by the theoretical heat transfer coefficient to 1 foot radius sphere at a surface temperature of 300K. Horvath et al. did not publish their theoretical stagnation heating rates, so the Newtonian velocity gradient method and tabulated air viscosity data were used to calculate theoretical stagnation heating rates in this paper. Horvath et al. ran the experiments at a low enough Reynolds number to expect laminar flow over the model; hence, the laminar boundary layer model is used in this paper. In addition, the initial wind tunnel model wall temperatures were not given. C_h is weakly a function of wall temperature. A wall temperature of 293K was assumed. Horvath et al. [49] calculated an experimental uncertainty of 15%, which is represented graphically with error bars in all figures.

A summary of the test conditions as well as the wind tunnel post-shock stagnation temperature T_0 and calculated theoretical stagnation heat transfer coefficient C_{h0} is given in Table 4. The first three cases were conducted in identical wind-tunnel conditions and at different angles of attack. The results are presented in Figure 19.

These three cases display different phenomena. The first case, where $\alpha = 0°$, uniformly underpredicts heating by approximately 15%. In the second case, HI-Mach underpredicts stagnation region heating by approximately 10% but overpredicts acreage heating by 10%. For the third case, HI-Mach again underpredicts stagnation region heating by approximately 10% and overpredicts acreage heating. However, the heating at the aft end is underpredicted. HI-Mach was run for these cases with a laminar boundary model, and the experimentally measured increase in heating at the aft end is likely due to boundary layer transition. In summary, these three cases demonstrate that HI-Mach compares favorably to experimental data within acceptable bounds for preliminary design.

Table 4. Summary of tested cases for HL-20 geometry. Reprinted with permission from Freeman et al. [2]. Copyright ©2025 Freeman.

	α (°)	M_∞	P_∞ (Pa)	ρ_∞ (kg/m^3)	T_0 (K)	C_{h0} (W/K cm^2)
Case 1	0	6.06	1965	0.1108	515.6	0.0170
Case 2	20	6.06	1965	0.1108	515.6	0.0170
Case 3	25	6.06	1965	0.1108	515.6	0.0170
Case 4	0	5.93	606.7	0.03355	506.11	0.00920
Case 5	0	10.04	223.4	0.01551	1019.4	0.0108
Case 6	25	5.93	606.7	0.03355	506.11	0.00920
Case 7	25	10.04	223.4	0.01551	1019.4	0.0108

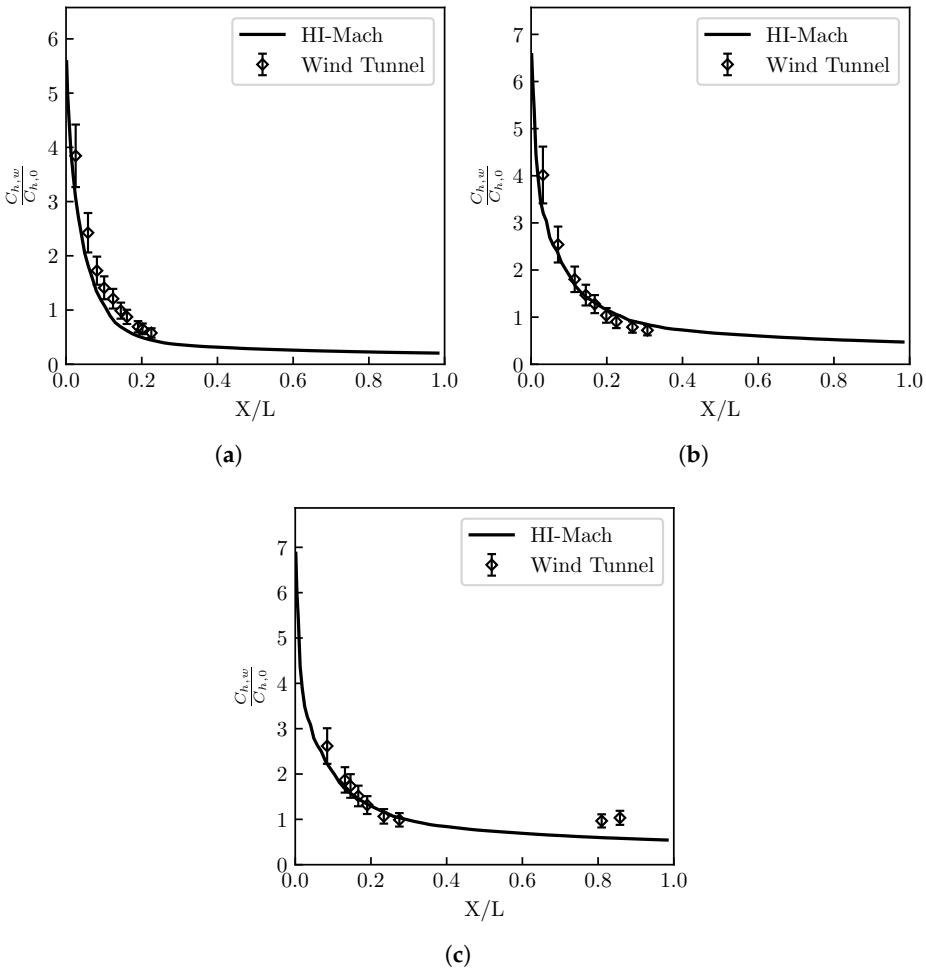
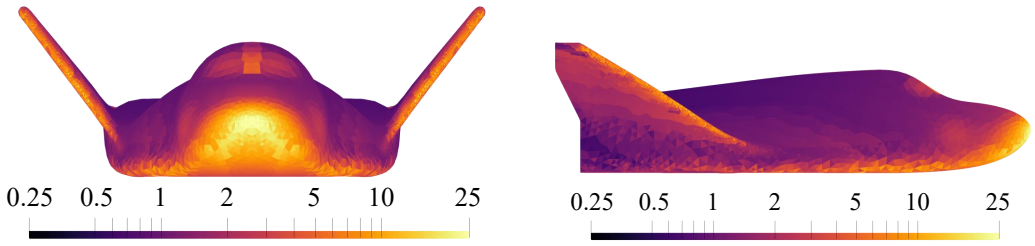


Figure 19. HL-20 windward centerline heating rate, comparison between wind tunnel and HI-Mach. Reprinted with permission from Freeman et al. [2]. Copyright ©2025 Freeman. (**a**) Case 1, $\alpha = 0°$, $M_\infty = 6.06$; (**b**) Case 2, $\alpha = 20°$, $M_\infty = 6.06$; (**c**) Case 3, $\alpha = 25°$, $M_\infty = 6.06$.

A surface-heating color contour plot for Case 2 is included to visualize the surface heating distribution (Figure 20). The heating rate is log-scaled. Note that the windward side for Case 2 is the lower surface.

The heating rate is highest in stagnation regions and along sharp attachment lines, such as on the leading edge of the fins. The heating rate decreases moving aft along the body. The models discussed and implemented in this paper operate on discrete meshes of triangles. In addition, the acreage heating directly depends on the stagnation region heating. An underprediction or overprediction of stagnation heating propagates through to the acreage heating production. Therefore, a poor-quality mesh will result in a poor

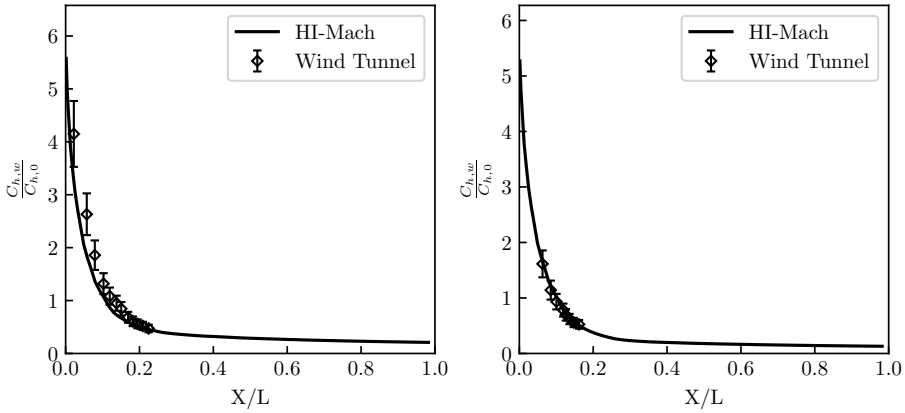
prediction of both stagnation and acreage heating. This effect is visible in Figure 20 in the streaks on the geometry.



(**a**) (**b**)

Figure 20. Surface heating rate $\dot{q}_w = (\mathrm{W/cm^2})$ contour plots on HL-20, Case 2: $\alpha = 20°$, $M_\infty = 6$. (**a**) Front; (**b**) Side. Adapted with permission from Freeman et al. [2]. Copyright ©2025 Freeman.

The fourth and fifth cases are at zero angle of attack and compare the heating rates at $M_\infty = 6$ and $M_\infty = 10$. The results are presented in Figure 21.



(**a**) (**b**)

Figure 21. HL-20 windward centerline heating rate, comparison between wind tunnel and HI-Mach. Reprinted with permission from Freeman et al. [2]. Copyright ©2025 Freeman. (**a**) Case 4, $\alpha = 0°$, $M_\infty = 5.93$; (**b**) Case 5, $\alpha = 0°$, $M_\infty = 10.04$.

In Case 4, HI-Mach underpredicts stagnation region heating by approximately 15%. This discrepancy could be due to a misprediction of the wall normal velocity gradient. However, the acreage heating prediction converges to the experimental values by $X/L = 0.25$. In Case 5, HI-Mach almost perfectly predicts both acreage and stagnation heating. The Modified Newtonian method is more accurate at higher Mach numbers.

The sixth and seventh cases are at a higher angle of attack, $\alpha = 25°$. Once again, these cases compare the heating rates at a higher angle of attack at Mach 6 and 10. The results are presented in Figure 22.

For Case 6, $\alpha = 25°$, $M_\infty = 6$, HI-Mach displays the same heating pattern as the wind tunnel measurements but underpredicts stagnation heating by approximately 10% and overpredicts acreage heating by the same factor. In Case 7, HI-Mach overpredicts heating in the stagnation and acreage regions. Despite small errors on the order of 10–15% in heating for the HL-20 across the seven cases, the good agreement exhibited between HI-Mach and wind tunnel measurements indicates that the code is a useful preliminary design tool. In addition, this tool runs extremely quickly with total calculation times on the order of 10 s on a standard desktop computer. The speed of this tool makes it very valuable for preliminary design work.

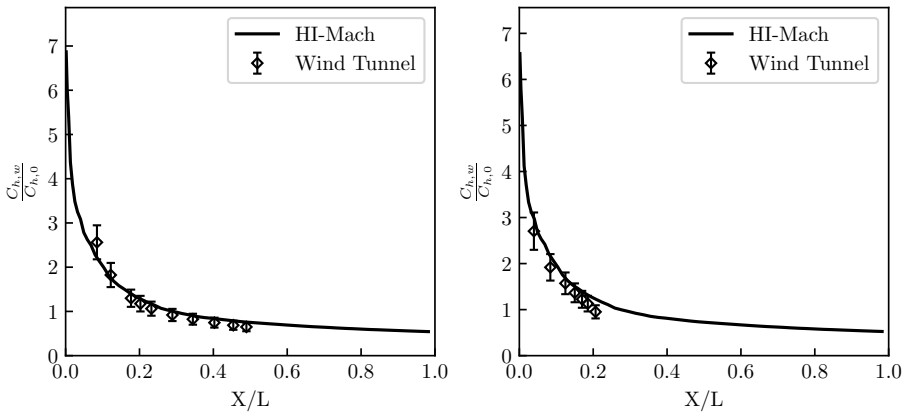


Figure 22. HL-20 windward centerline heating rate, comparison between wind tunnel and HI-Mach. Reprinted with permission from Freeman et al. [2]. Copyright ©2025 Freeman. (**a**) Case 4, $\alpha = 25°$, $M_\infty = 5.93$; (**b**) Case 5, $\alpha = 25°$, $M_\infty = 10.04$.

3.3. Sensitivities

This section examines the results of the sensitivity methods presented in this paper. First, a comparison is made with finite differencing to show correct implementation. Second, a runtime comparison is made between direct differentiation and finite differencing. Lastly, a representative result of derivatives is shown on the HL-20. A simple case study pairing the methods here with Engineering Sketch Pad for a simple geometry is shown in [3].

3.3.1. Finite Difference Comparison

Each of the sensitivities in HI-Mach was compared with finite differencing to ensure correct derivation and implementation. Central differencing was used where each geometry point was perturbed in a coordinate direction and the quantity of interest was evaluated. This results in $6n$ runs of the base solver to find the derivative of the quantity of interest. The step size was determined by examining the truncation and round-off error for varying step sizes. Figure 23 shows the error of the central difference method compared to the direct method.

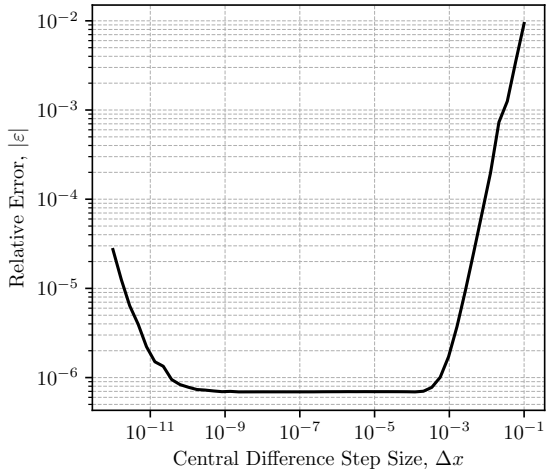


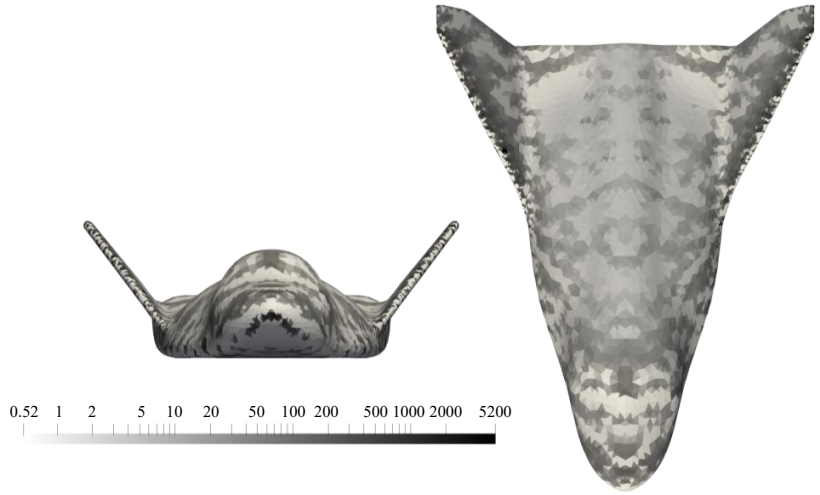
Figure 23. Relative error of central difference method compared to direct method for derivative of lift coefficient.

The central difference step size chosen for verification is in the region where neither truncation nor round-off error dominates. The step size was chosen as the cube root of machine precision for an 8-byte floating point number, $h = \sqrt[3]{\epsilon_{\text{machine}}} = 6.055 \times 10^{-6}$.

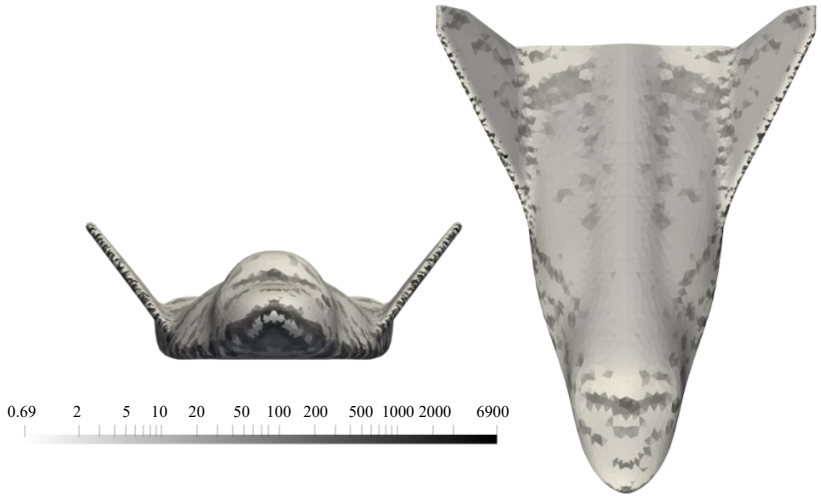
There are some cases within HI-Mach in which a quantity of interest is not a continuous function of geometry. For example, as geometry perturbations increase in magnitude, one might expect some streamlines to change their path discontinuously as they reach the edge of panels. Computation of the direct derivative assumes that the computational path does not change. In validating this method with finite difference, it is essential to make the step size small enough to not change the computational path.

3.3.2. Representative Case

The sensitivity of the total heat load to the HL-20 body was computed. A representative result is included below in Figure 24. To display it, the sensitivity was computed in the direction of the vertex normal vectors. Therefore, a positive value on the surface contour plot indicates that moving the vertex 'out' would result in an increased total heat load. A negative value on the contour plot indicates that moving the vertex 'in' would result in a decreased total heat load.



(**a**)



(**b**)

Figure 24. Separated derivative of total heat load onto the vehicle, $\left|\frac{\partial q_{\text{load}}}{\partial \chi}\right|$. (**a**) Positive component: $\text{sgn}\left(\frac{\partial q_{\text{load}}}{\partial \chi}\right) > 0$. Moving these panels out increases the total heat load. (**b**) Negative component: $\text{sgn}\left(\frac{\partial q_{\text{load}}}{\partial \chi}\right) < 0$. Moving these panels out decreases the total heat load.

The data in Figure 24 are scaled logarithmically. From the figure, the highest magnitude areas are on the nose, chines, and fins. These are attachment areas, which are subject to higher heating magnitudes than acreage areas. In addition, a high heat rate in an attachment region transmits downstream and increases acreage heating. The result that total heating sensitivity is highest in attachment regions is expected from the theory and observed in Figure 24.

It can also be seen that pulling in the tip of the nose and pushing out the surrounding panels would decrease the total heat load. The result agrees with the classic Allen and Eggers law that blunting the nose of a hypersonic vehicle reduces the heating.

3.3.3. Runtime Comparison

The simplest way to calculate the sensitivities of performance quantities such as lift, drag, and temperature with respect to the geometry is through finite differencing. First, the solution is run without perturbing any points. Then, a point on the geometry is perturbed and the solution is re-run. Three perturbations are required for each point on the geometry for a first-order forward- or backward-difference approach. Six perturbations are required for a central difference approach. Therefore, $6n$ complete solutions are required to compute the shape sensitivities of a geometry with central differencing. The prohibitive cost of central differencing is part of the motivation for directly calculating the shape sensitivities.

The runtime of a central difference method for calculating sensitivities will be compared to the runtime using the approach described in this paper. When running finite differencing, different approaches can be taken to minimize the run time. The simplest approach would be to run HI-Mach start to finish $6n$ times. However, with that approach, the surface mesh is loaded from file every time, which is slow.

Another example would be applying a heuristic and deciding which vertices to central difference against. For example, when calculating the properties after perturbing a vertex on the upper surface of an aircraft, the bottom surface is not affected, and so it is only necessary to recalculate the top surface.

In making this central difference comparison, the authors decided to time only the calculation period of the code, excluding any file reading and writing. No heuristics were used in the finite differencing, since these are not known a priori and thus make an unfair comparison.

The timings were performed on spheres and Sears–Haack bodies of varying vertex count. At higher vertex counts, it is prohibitively expensive to run $6n$ cases for central differencing. Instead, the code execution was timed and averaged for a smaller number of runs and extrapolated. The run settings which affect the execution time of the code are provided below:

- Wall Temperature: Radiation Equilibrium;
- Attachment Line Detection: Eigenvalue and Streamline Tracing;
- Boundary Layer Model: Laminar;
- Gas Data: Tabulated;
- Streamline Density: Sparse.

The settings were maintained for both the finite differencing and direct runs of the code.

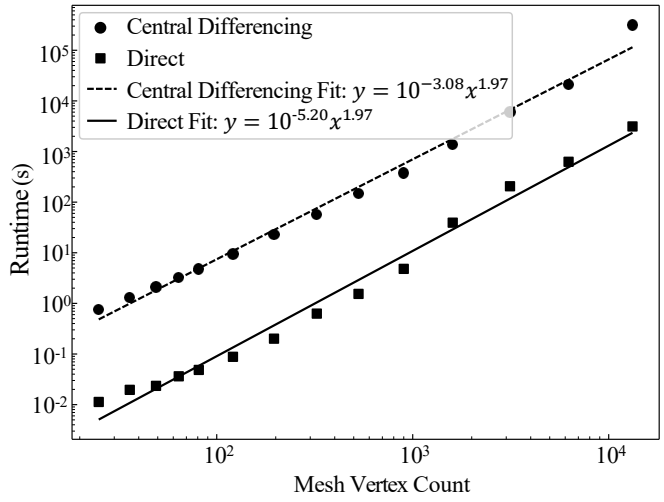
The timing comparisons were performed on an i9-12900H with 64 Gb of DDR5 memory. Multithreading options exist for HI-Mach both in the base and derivative form. However, to ensure a fair timing comparison, the code was compiled to run on a single thread. The runtime comparisons on a sphere and Sears–Haack body are shown in Figure 25.

Figure 25 demonstrates interesting results. The direct method of calculating derivatives is approximately two orders of magnitude faster than central differencing. Based on the scaling, central differencing on large meshes (more than 10,000 mesh vertices) takes more

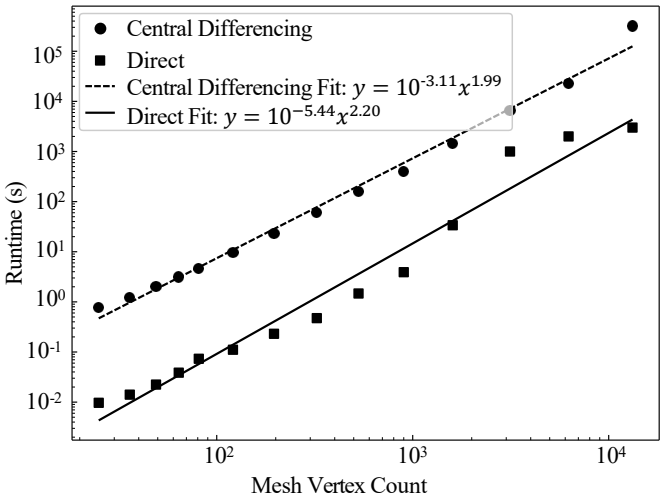
than a day. In comparison, the direct method can execute a 10,000 vertex mesh in less than an hour.

One interesting aspect is the scaling. Both the central differencing and direct methods appear to have approximately $\mathcal{O}(n^2)$ scaling. In both methods, the most computationally expensive aspect is computing the streamlines (and the sensitivity of the streamlines). In Navier–Stokes CFD, the adjoint (or sensitivity) can be computed for the same cost as the base solution. Therefore, computing the sensitivities with the adjoint method in CFD scales better than computing them with finite differencing. However, computing the sensitivity in this panel method scales the same as finite differencing, which is offset by a finite cost. This agrees with the scaling results found by Hoch in a supersonic panel code [50].

Departures from $\mathcal{O}(n^2)$ are observed. Some of the deviation is likely due to memory effects. The direct derivative method stores multiple arrays of size $m \times n$, so its memory scaling is approximately $\mathcal{O}(n^2)$. RAM access speed is non-linear. Large slowdowns were observed during the scaling study and attributed to large memory requirements.



(**a**)



(**b**)

Figure 25. Runtime comparisons for sphere and Sears–Haack geometry between central-differencing and direct derivative calculation. (**a**) Sphere; (**b**) Sears–Haack.

4. Conclusions

This paper has presented the development of an engineering level code, HI-Mach, for calculating hypersonic aerodynamics and convective heating along with their geometric sensitivities. Independent panel inclination methods are used to calculate the pressure distribution on the surface of a hypersonic vehicle. Various methods are available for the calculation of surface pressures on the surface of an arbitrary hypersonic vehicle. Normal shock relations provide the thermodynamic state on each panel. Surface streamlines are integrated from panel to panel using closed-form streamline equations. The application of a sparse streamline tracing method improves the computation time with relatively small decreases in accuracy. Flat-plate formulas corrected for compressibility are used to calculate the skin friction coefficient on each panel.

Methods based on impact theory are used to approximate the surface convective heating on a vehicle in hypersonic flow. These methods are implemented into HI-Mach to predict aeroheating on an unstructured surface grid. Detailed methodology for calculating surface convective heat fluxes is presented and discussed, including methods for calculating heating inside and outside of stagnation regions. Two approaches to estimate the surface curvature from discretized, unstructured triangle meshes are discussed and compared. The implementation of wall conditions is discussed and verified. Radiative heating from the surrounding gases is not considered. This limits the applicability to moderate hypersonic regimes.

The calculation of sensitivities of quantities of interest such as heat flux, lift, and drag are useful for optimizing a hypersonic design. These sensitivities can be derived analytically for a hypersonic impact method. An approach to obtain the sensitivities of the present methods is explored and derived. Direct analytical sensitivities are obtained where possible. For difficult calculations such as curvature, an alternative approach to obtaining the sensitivities is described.

Results from HI-Mach are compared against published wind tunnel and analytical results for the HL-20 hypersonic lifting body. For the aerodynamic cases considered, HI-Mach predicted the force coefficients within 21%. The error between HI-Mach and the experimental results decreased as the Mach number increased. Results from the present heating implementation are compared with experimental results for the HL-20 for different freestream conditions. Agreement with these results is generally accurate to within 15%. Areas where HI-Mach does not match published data well give direction for further work. These include real-gas effects at high-speed flight conditions and the prediction of turbulent transition.

As mentioned previously, the methods developed in this paper are similar to those used in CBAERO and HABP with differences mostly arising from the unique contributions of this paper, which include novel streamline tracing and direct sensitivities. A direct comparison of results from the methods presented here to those from CBAERO and HABP was not included. Rather, this paper focused on comparing results of the present methodology to theoretical/analytic solutions and experimental results. Further studies could be performed to compare the accuracy of the present methods to those from similar methods such as CBAERO and HABP

The calculated geometric sensitivities for heat loads on the HL-20 follow expected trends. A study of the computation of sensitivities demonstrates that the sensitivities are of computational complexity $\mathcal{O}(n^2)$. Compared to finite differencing, the method presented in this paper is approximately two orders of magnitude faster.

To date, HI-Mach has been used by Ford and Hunsaker for trajectory optimization [15] and by Weaver and Hunsaker for waverider shape optimization [16]. Extremely low

calculation times provided by HI-Mach enable Ford, Weaver, and others to conduct quick trade studies and analyses across a broad range of conditions.

HI-Mach allows initial estimates of aerodynamic forces and heat loads at high speed and low computational cost. Execution times on laptops and basic workstations are orders of magnitude faster than CFD. The methods and approaches presented here allow for the agile development and optimization of hypersonic vehicles.

Author Contributions: Conceptualization, J.G., L.F., N.H. and D.H.; Methodology, J.G., L.F., N.H. and D.H.; Software, J.G. and L.F.; Validation, J.G., L.F.; Writing—original draft, J.G. and L.F.; Writing—review & editing, J.G.; Supervision, N.H. and D.H.; Project administration, D.H.; Funding acquisition, D.H. All authors have read and agreed to the published version of the manuscript.

Funding: This work was funded by the Air Force AFWERX STTR Contract number FA864923P1213 with Jose Camberos as the Technical Point of Contact.

Data Availability Statement: The original contributions presented in this study are included in the article. Further inquiries can be directed to the corresponding author.

Conflicts of Interest: The authors declare no conflicts of interest.

Nomenclature

a, b, c	velocity distribution constants
A	signed area of triangle
A_{ref}	boody reference area
$[A_{g\to l}]$	panel coordinate transformation matrix
B_1, B_2	streamline constants
$\hat{\boldsymbol{c}}$	panel centroid vector
c_f	skin friction coefficient
C_F	body force coefficient vector
C_H	Newton's law of cooling heat transfer coefficient
$\overline{C_H}$	non-dimensional heat transfer coefficient
$C_i \quad i = \{1, 6\}$	tangent cone polynomial constants
C_D	drag coefficient
C_L	lift coefficient
C_M	body moment coefficient vector
C_P	pressure coefficient
$C_{P_{\text{max}}}$	maximum pressure coefficient
$\boldsymbol{e}$	edge vector between vertices
$[E]$	eigenvector matrix
h	specific enthalpy
k_{geom}	geometric heating factor
k_{c_f}	skin friction factor
l_{ref}	body reference length
Le	Lewis number
m_{mol}	molar mass
m	number of mesh panels
M	Mach number
M_f	Mangler factor
n	number of mesh vertices
$\hat{\boldsymbol{n}}$	surface unit normal vector
$\boldsymbol{p}$	vertex coordinates
P	pressure
Pr	Prandtl number

$\dot{q}$	surface heating rate
r	recovery factor
R	radius of curvature
$[R]$	barycentric coordinate transform matrix
R_U	universal gas constant
Re_x	running length Reynolds number
Re_T	transition Reynolds number
S	Sutherland constant
$\boldsymbol{S}$	shape operator
s	Reynolds analogy factor
T	temperature
u	velocity in the x direction
v	velocity in the y direction
$\hat{\boldsymbol{V}}_\infty$	freestream velocity vector
$\hat{\boldsymbol{v}}_\infty$	freestream direction unit vector
$\hat{\boldsymbol{v}}_A$	panel velocity direction unit vector
$\boldsymbol{V}$	velocity vector
V_r	cone surface velocity
V_θ	cone radial velocity
x	total running length
x_i	single panel running length
$\hat{x}_i$	panel streamline end point
$\hat{x}_{i-1}$	panel streamline start point
x_{cp}, y_{cp}	critical point location
X, Y	eigenvector axes
β	shock angle
$\beta_{\max}$	maximum shock angle
γ	ratio of specific heats
δ	shock strength indicator
Δ	shock standoff distance
$\bar{\Delta}$	shock standoff distance non-dimensionalized by radius of curvature
ϵ	surface emissivity
$\boldsymbol{\chi}$	discretized mesh represented as a column vector of all vertex coordinates
Γ	boundary layer transition factor
κ	curvature
λ	eigenvalue
Λ	barycentric coordinates
Λ	sweep angle
ρ	density
σ	Stefan-Boltzmann constant
θ	panel inclination
$\theta_{\max}$	maximum inclination angle
τ	shear stress
ψ, ϕ	oblique shock function
r, φ	Taylor–Maccoll cone coordinates
μ	dynamic viscosity
ν	Prandtl–Meyer function
ξ, η	eigenvectors

ζ, ϑ	local coordinates
$\boldsymbol{\zeta}, \boldsymbol{\vartheta}$	local coordinate system directions

Subscripts

0	stagnation property
2	post-shock property
aw	adiabatic wall property
e	boundary layer edge property
i	surface face property
j	streamline intersection edge index
L	laminar boundary layer
ref	reference property
T	turbulent boundary layer
TR	boundary layer transition property
w	wall property
∞	freestream property
1	maximum principal
2	minimum principal
attach, perp	curvature in the attachment line direction and perpendicular to that

Superscripts

$*$	property evaluated at reference temperature
l	local panel coordinates

Appendix A. Intermediate Derivatives

This appendix contains intermediate derivatives necessary for the calculation of sensitivities in HI-Mach.

Appendix A.1. Additional Definitions

In this paper, the derivative of a vector dot product or vector cross-product is computed. For a dot product, the derivative is of the form

$$\frac{\partial(\boldsymbol{a} \cdot \boldsymbol{b})}{\partial \boldsymbol{\chi}} = \frac{\partial \boldsymbol{a}}{\partial \boldsymbol{\chi}} \cdot \boldsymbol{b} + \boldsymbol{a} \cdot \frac{\partial \boldsymbol{b}}{\partial \boldsymbol{\chi}} \tag{A1}$$

The terms on the right-hand side are technically Jacobian-vector products—not vector dot products. Taking the derivative of $\boldsymbol{a}$ or $\boldsymbol{b}$ with respect to $\boldsymbol{\chi}$, a vector, results in a Jacobian. However, in this paper, these derivative matrix-vector products are left in dot product form. Similarly, for a cross-product, the derivative is of the form

$$\frac{\partial(\boldsymbol{a} \times \boldsymbol{b})}{\partial \boldsymbol{\chi}} = \frac{\partial \boldsymbol{a}}{\partial \boldsymbol{\chi}} \times \boldsymbol{b} + \boldsymbol{a} \times \frac{\partial \boldsymbol{b}}{\partial \boldsymbol{\chi}} \tag{A2}$$

The right-hand side terms are technically matrix products, since taking the cross-product of a matrix with a vector is not well defined. Functionally, this operation is equivalent to row-wise cross-products. The notation is left unmodified throughout this paper for convenience.

Appendix A.2. Intermediate Geometric Derivatives

The derivative of a vertex position with respect to the set of vertex coordinates is a $3 \times n$ matrix. For the n-th vertex position, the derivative is

$$\frac{\partial \mathbf{p}_n}{\partial \chi} = \begin{bmatrix} 0 & 0 & 0 \\ \vdots & \vdots & \vdots \\ 1 & 0 & 0 \\ 0 & 0 & 0 \\ \vdots & \vdots & \vdots \\ 0 & 1 & 0 \\ 0 & 0 & 0 \\ \vdots & \vdots & \vdots \\ 0 & 0 & 1 \end{bmatrix}^{T} \tag{A3}$$

The derivative of a panel edge with respect to the coordinate vector is

$$\frac{\partial \mathbf{e}_{ij}}{\partial \chi} = \frac{\partial \mathbf{p}_j}{\partial \chi} - \frac{\partial \mathbf{p}_i}{\partial \chi} \tag{A4}$$

which is also a $3 \times n$ matrix. It is useful to define the edge normal vector by

$$\hat{\mathbf{e}}_{ij} = \frac{\mathbf{e}_{ij}}{|\mathbf{e}_{ij}|} \tag{A5}$$

The derivative of the edge vector magnitude is

$$\frac{\partial |\mathbf{e}_{ij}|}{\partial \chi} = \frac{1}{2|\mathbf{e}_{ij}|} \frac{\partial}{\partial \chi} (\mathbf{e}_{ij} \cdot \mathbf{e}_{ij}) = \frac{1}{|\mathbf{e}_{ij}|} \left(\frac{\partial \mathbf{e}_{ij}}{\partial \chi} \right) \mathbf{e}_{ij} = \left(\frac{\partial \mathbf{e}_{ij}}{\partial \chi} \right) \cdot \hat{\mathbf{e}}_{ij} \tag{A6}$$

Using this definition, the derivative of the edge normal vector can be expressed as

$$\frac{\partial \hat{\mathbf{e}}_{ij}}{\partial \chi} = \frac{|\mathbf{e}_{ij}| \frac{\partial \mathbf{e}_{ij}}{\partial \chi} - \frac{\partial |\mathbf{e}_{ij}|}{\partial \chi} \mathbf{e}_{ij}}{\mathbf{e}_{ij} \cdot \mathbf{e}_{ij}} \tag{A7}$$

which is a $3 \times n$ matrix. A panel unit normal vector is defined by

$$\hat{\mathbf{n}} = \frac{\mathbf{e}_{ij} \times \mathbf{e}_{jk}}{|\mathbf{e}_{ij} \times \mathbf{e}_{jk}|} \tag{A8}$$

The derivative of the panel unit normal with respect to the coordinates is then obtained as

$$\frac{\partial \hat{\mathbf{n}}}{\partial \chi} = \frac{|\mathbf{e}_{ij} \times \mathbf{e}_{jk}| \left[\left(\mathbf{e}_{ij} \times \frac{\partial \mathbf{e}_{jk}}{\partial \chi} \right) + \left(\frac{\partial \mathbf{e}_{ij}}{\partial \chi} \times \mathbf{e}_{jk} \right) \right] - \frac{\partial}{\partial \chi} \left(|\mathbf{e}_{ij} \times \mathbf{e}_{jk}| \right) \mathbf{e}_{ij} \times \mathbf{e}_{jk}}{\left(\mathbf{e}_{ij} \times \mathbf{e}_{jk} \right) \cdot \left(\mathbf{e}_{ij} \times \mathbf{e}_{jk} \right)} \tag{A9}$$

where

$$\frac{\partial}{\partial \chi} \left(|\mathbf{e}_{ij} \times \mathbf{e}_{jk}| \right) = \left[\left(\mathbf{e}_{ij} \times \frac{\partial \boldsymbol{e}_{jk}}{\partial \chi} \right) + \left(\frac{\partial \mathbf{e}_{ij}}{\partial \chi} \times \mathbf{e}_{jk} \right) \right] \cdot \frac{\mathbf{e}_{ij} \times \mathbf{e}_{jk}}{|\mathbf{e}_{ij} \times \mathbf{e}_{jk}|} \tag{A10}$$

This is also a $3 \times n$ matrix.

Appendix A.3. Intermediate Inviscid Pressure Derivatives

Appendix A.3.1. Tangent Wedge

The chain rule gives

$$\frac{\partial \beta}{\partial \chi} = \frac{\partial \beta}{\partial \theta} \frac{\partial \theta}{\partial \chi} \tag{A11}$$

where

$$\frac{\partial \beta}{\partial \theta} = \frac{\frac{2\cos\left(\frac{4\pi}{3}+\frac{\operatorname{acos}(\phi)}{3}\right)\frac{\partial}{\partial\theta}\psi + \frac{2\sin\left(\frac{4\pi}{3}+\frac{\operatorname{acos}(\phi)}{3}\right)\psi\frac{\partial}{\partial\theta}\phi}{3\sqrt{1-\phi^2}}}{\tan(\theta)\left(3M^2\left(\frac{\gamma-1}{2}\right)+3\right)} - \frac{\left(\tan(\theta)^2+1\right)\left(M^2+2\cos\left(\frac{4\pi}{3}+\frac{\operatorname{acos}(\phi)}{3}\right)\psi-1\right)}{\tan(\theta)^2\left(3M^2\left(\frac{\gamma-1}{2}\right)+3\right)}}{\frac{\left(M^2+2\cos\left(\frac{4\pi}{3}+\frac{\operatorname{acos}(\phi)}{3}\right)\psi-1\right)^2}{\tan(\theta)^2\left(3M^2\left(\frac{\gamma-1}{2}\right)+3\right)^2}+1} \tag{A12}$$

The variables ψ and ϕ are given in Equations (7) and (8), and their partial derivatives with respect to θ are

$$\frac{\partial \psi}{\partial \theta} = -\frac{\tan(\theta)\left(\left(\frac{\gamma+1}{2}\right)M^2+1\right)\left(3M^2\left(\frac{\gamma-1}{2}\right)+3\right)\left(\tan(\theta)^2+1\right)}{\sqrt{\left(M^2-1\right)^2-\tan(\theta)^2\left(\left(\frac{\gamma+1}{2}\right)M^2+1\right)\left(3M^2\left(\frac{\gamma-1}{2}\right)+3\right)}} \tag{A13}$$

and

$$\frac{\partial \phi}{\partial \theta} = -\frac{3\left(\left(M^2-1\right)^3-\tan^2\theta\left(9M^2\left(\frac{\gamma-1}{2}\right)+9\right)\left(\left(\frac{\gamma+1}{4}\right)M^4+\left(\frac{\gamma-1}{2}\right)M^2+1\right)\right)\frac{\partial\psi}{\partial\theta}}{\psi^4} - \frac{2\tan\theta\left(9M^2\left(\frac{\gamma-1}{2}\right)+9\right)\left(\tan^2\theta+1\right)\left(\left(\frac{\gamma+1}{4}\right)M^4+\left(\frac{\gamma-1}{2}\right)M^2+1\right)}{\psi^3} \tag{A14}$$

Appendix A.3.2. Prandtl–Meyer Expansion

The first term in the chain rule sequence is obtained by the application of derivative rules, resulting in

$$\frac{\partial C_{p,\text{expansion}}}{\partial M} = -\frac{2M}{M_\infty^2}\left(\frac{1+\frac{\gamma-1}{2}M_\infty^2}{1+\frac{\gamma-1}{2}M^2}\right)^{\frac{1}{\gamma-1}}\left(\frac{1+\frac{\gamma-1}{2}M_\infty^2}{\left(1+\frac{\gamma-1}{2}M^2\right)^2}\right) \tag{A15}$$

The second term involves the Mach number relation, which is governed by the Prandtl–Meyer relation given as

$$\theta = \nu(M) - \nu(M_\infty) \tag{A16}$$

Therefore, the Mach number on the expansion surface can be expressed as

$$M = \nu^{-1}(\theta + \nu(M_\infty)) \tag{A17}$$

where $\nu^{-1}(\theta)$ denotes the inverse Prandtl–Meyer function, which is impossible to express in terms of elementary functions. Nevertheless, by differentiating, we arrive at

$$\frac{\partial M}{\partial \theta} = \frac{\partial}{\partial \theta}\nu^{-1}(\theta + \nu(M_\infty)) \tag{A18}$$

which can be expressed using the inverse derivative rule as

$$\frac{\partial M}{\partial \theta} = \frac{1}{\nu'(\nu^{-1}(\theta + \nu(M_\infty)))} \tag{A19}$$

where the derivative of the Prandtl–Meyer function is

$$\nu'(M) = \frac{\partial \nu(M)}{\partial M} = \frac{M\sqrt{\frac{\gamma+1}{\gamma-1}}(\gamma-1)}{\sqrt{\frac{(M^2-1)(\gamma-1)}{\gamma+1}}(M^2\gamma-M^2+2)} - \frac{1}{M\sqrt{M^2-1}} \tag{A20}$$

The expression for the derivative of the Mach number with respect to θ still involves the inverse Prandtl–Meyer function, which cannot be directly calculated. However, the

quantity $\nu^{-1}(\theta + \nu(M_\infty))$ is the Mach number on the expansion surface, which is already computed. In this implementation, the inverse Prandtl–Meyer function is evaluated based on a table lookup.

Appendix A.4. Intermediate Stagnation Heating Derivatives

Velocity Gradient

As shown previously, there are multiple approaches to calculating the boundary layer edge velocity gradient, and the derivative is different for each approach. The velocity gradient depends on the surface curvature. The Olivier velocity gradient method is used as a default in HI-Mach. The derivative of the Olivier velocity gradient is

$$\frac{\partial}{\partial \chi}\left(\frac{du_e}{dx}\right) = \frac{u_\infty}{\rho_\infty u_\infty^2 \rho_s}\frac{1+\overline{\Delta}}{\overline{\Delta}}\left[-\frac{1}{R^2}\frac{\partial R}{\partial \chi}(P_0 - P_2)\rho_2\right] \tag{A21}$$

where the derivative of the radius is related to curvature derivatives through

$$\frac{\partial R}{\partial \chi} = -\frac{1}{\kappa_{\text{perp}}^2}\frac{\partial \kappa_{\text{perp}}}{\partial \chi} \tag{A22}$$

The curvature in the direction perpendicular to the attachment line, κ_{perp}, is related to the principal curvatures through

$$\kappa_{\text{attach}} = \cos^2\theta(\kappa_1 - \kappa_2) + \kappa_2 \tag{A23}$$

$$\kappa_{\text{perp}} = \kappa_1 + \kappa_2 - \kappa_{\text{attach}} \tag{A24}$$

where θ is the angle between the attachment line direction and the first principal direction of curvature. The $\cos^2\theta$ term and its derivative are given by

$$\cos^2\theta = \left(\hat{\boldsymbol{\xi}}_1 \cdot \hat{\boldsymbol{a}}_L\right)^2; \quad \frac{\partial \cos^2\theta}{\partial \chi} = 2\left(\hat{\boldsymbol{\xi}}_1 \cdot \hat{\boldsymbol{a}}_L\right)\left(\frac{\partial \hat{\boldsymbol{\xi}}_1}{\partial \chi}\cdot \hat{\boldsymbol{a}}_L + \hat{\boldsymbol{\xi}}_1 \cdot \frac{\partial \hat{\boldsymbol{a}}_L}{\partial \chi}\right) \tag{A25}$$

where the principal curvature direction $\hat{\boldsymbol{\xi}}_1$ and the attachment line direction $\hat{\boldsymbol{a}}_L$ are assumed to be unit vectors. The derivative of curvature in the attachment direction is the

$$\frac{\partial \kappa_{\text{attach}}}{\partial \chi} = \frac{\partial \cos^2\theta}{\partial \chi}(\kappa_1 - \kappa_2) + \cos^2\theta\left(\frac{\partial \kappa_1}{\partial \chi} - \frac{\partial \kappa_2}{\partial \chi}\right) + \frac{\partial \kappa_2}{\partial \chi} \tag{A26}$$

which leads to an expression for the derivative of the curvature in the perpendicular direction

$$\frac{\partial \kappa_{\text{perp}}}{\partial \chi} = \frac{\partial \kappa_1}{\partial \chi} + \frac{\partial \kappa_2}{\partial \chi} - \frac{\partial \kappa_{\text{attach}}}{\partial \chi} \tag{A27}$$

Appendix A.5. Intermediate Running Length Derivatives

The end point of the panel is determined using an intersection between an inner and outer streamline point and the panel edge as described earlier. Thus, the sensitivity of the endpoint of each streamline on a panel is given as

$$\begin{aligned}\frac{\partial \hat{x}_i}{\partial \chi} = &-\frac{\partial \Lambda_j(\hat{x}_{out})}{\partial \chi}\frac{\hat{x}_{in} - \hat{x}_{out}}{\Lambda_j(\hat{x}_{in}) - \Lambda_j(\hat{x}_{out})} \\ &- \Lambda_j(\hat{x}_{out})\frac{\left(\Lambda_j(\hat{x}_{in}) - \Lambda_j(\hat{x}_{out})\right)\left(\frac{\partial \hat{x}_{in}}{\partial \chi} - \frac{\partial \hat{x}_{out}}{\partial \chi}\right) - \left(\frac{\partial \Lambda_j(\hat{x}_{in})}{\partial \chi} - \frac{\partial \Lambda_j(\hat{x}_{out})}{\partial \chi}\right)(\hat{x}_{in} - \hat{x}_{out})}{\left(\Lambda_j(\hat{x}_{in}) - \Lambda_j(\hat{x}_{out})\right)^2} + \frac{\partial \hat{x}_{out}}{\partial \chi}\end{aligned} \tag{A28}$$

where the sensitivities of the barycentric coordinates are calculated by

$$\frac{\partial[\Lambda]}{\partial \chi} = [R]^{-1}\begin{Bmatrix} 0 \\ \frac{\partial x}{\partial \chi} \\ \frac{\partial y}{\partial \chi} \end{Bmatrix} - [R]^{-1}\frac{\partial[R]}{\partial \chi}[R]^{-1}\begin{Bmatrix} 1 \\ x \\ y \end{Bmatrix}. \tag{A29}$$

The sensitivities of the outer and inner points can be can be calculated by inputting the respective parameters t_{out} and t_{in} into

$$\frac{\partial \hat{x}}{\partial \chi} = \frac{\partial}{\partial \chi}\begin{bmatrix} \xi_1 & \eta_1 \\ \xi_2 & \eta_2 \end{bmatrix}\begin{Bmatrix} B_1 e^{\lambda_1 t} \\ B_2 e^{\lambda_2 t} \end{Bmatrix} + \begin{bmatrix} \xi_1 & \eta_1 \\ \xi_2 & \eta_2 \end{bmatrix}\begin{Bmatrix} \frac{\partial B_1}{\partial \chi} e^{\lambda_1 t} + B_1\left(\frac{\partial \lambda_1}{\partial \chi} t\right) e^{\lambda_1 t} \\ \frac{\partial B_2}{\partial \chi} e^{\lambda_2 t} + B_2\left(\frac{\partial \lambda_2}{\partial \chi} t\right) e^{\lambda_2 t} \end{Bmatrix} + \begin{Bmatrix} \frac{\partial x_{cp}}{\partial \chi} \\ \frac{\partial y_{cp}}{\partial \chi} \end{Bmatrix} \tag{A30}$$

where

$$\frac{\partial}{\partial \chi}\begin{Bmatrix} B_1 \\ B_2 \end{Bmatrix} = -[E]^{-1}\frac{\partial[E]}{\partial \chi}[E]^{-1}\begin{bmatrix} x^l_{i-1} - x_{cp} \\ y^l_{i-1} - y_{cp} \end{bmatrix} + [E]^{-1}\begin{Bmatrix} \frac{\partial x^l_{i-1}}{\partial \chi} - \frac{\partial x_{cp}}{\partial \chi} \\ \frac{\partial y^l_{i-1}}{\partial \chi} - \frac{\partial y_{cp}}{\partial \chi} \end{Bmatrix} \tag{A31}$$

$$\frac{\partial \lambda}{\partial \chi} = \frac{\partial b_1}{\partial \chi} + \frac{\partial c_2}{\partial \chi} \pm \frac{2(b_1 + c_2)(\frac{\partial b_1}{\partial \chi} + \frac{\partial c_2}{\partial \chi}) - 4\left(\frac{\partial b_1}{\partial \chi} c_2 + b_1 \frac{\partial c_2}{\partial \chi} - \frac{\partial b_2}{\partial \chi} c_1 - b_2 \frac{\partial c_1}{\partial \chi}\right)}{4\sqrt{(b_1 + c_2)^2 - 4(b_1 c_2 - b_2 c_1)}} \tag{A32}$$

$$\frac{\partial}{\partial \chi}\begin{Bmatrix} \xi_1 \\ \xi_2 \end{Bmatrix} = \begin{Bmatrix} \frac{\partial \lambda_1}{\partial \chi} - \frac{\partial c_2}{\partial \chi} \\ \frac{\partial c_1}{\partial \chi} \end{Bmatrix} \text{ or } \begin{Bmatrix} \frac{\partial b_2}{\partial \chi} \\ \frac{\partial \lambda_1}{\partial \chi} - \frac{\partial b_1}{\partial \chi} \end{Bmatrix} \tag{A33}$$

$$\frac{\partial}{\partial \chi}\begin{Bmatrix} \eta_1 \\ \eta_2 \end{Bmatrix} = \begin{Bmatrix} \frac{\partial \lambda_2}{\partial \chi} - \frac{\partial c_2}{\partial \chi} \\ \frac{\partial c_1}{\partial \chi} \end{Bmatrix} \text{ or } \begin{Bmatrix} \frac{\partial b_2}{\partial \chi} \\ \frac{\partial \lambda_2}{\partial \chi} - \frac{\partial b_1}{\partial \chi} \end{Bmatrix} \tag{A34}$$

$$\frac{\partial x_{cp}}{\partial \chi} = \frac{(b_1 c_2 - b_2 c_1)\left(\frac{\partial a_2}{\partial \chi} c_1 + a_2 \frac{\partial c_1}{\partial \chi} - \frac{\partial a_1}{\partial \chi} c_2 - a_1 \frac{\partial c_2}{\partial \chi}\right) - (a_2 c_1 - a_1 c_2)\left(\frac{\partial b_1}{\partial \chi} c_2 + b_1 \frac{\partial c_2}{\partial \chi} - \frac{\partial b_2}{\partial \chi} c_1 - b_2 \frac{\partial c_1}{\partial \chi}\right)}{(b_1 c_2 - b_2 c_1)^2} \tag{A35}$$

$$\frac{\partial y_{cp}}{\partial \chi} = \frac{(b_1 c_2 - b_2 c_1)\left(\frac{\partial a_1}{\partial \chi} b_2 + a_1 \frac{\partial b_2}{\partial \chi} - \frac{\partial a_2}{\partial \chi} b_1 - a_2 \frac{\partial b_1}{\partial \chi}\right) - (a_1 b_2 - a_2 b_1)\left(\frac{\partial b_1}{\partial \chi} c_2 + b_1 \frac{\partial c_2}{\partial \chi} - \frac{\partial b_2}{\partial \chi} c_1 - b_2 \frac{\partial c_1}{\partial \chi}\right)}{(b_1 c_2 - b_2 c_1)^2} \tag{A36}$$

Appendix A.6. Intermediate Velocity Derivatives

First, evaluating $\frac{\partial\{S\}}{\partial \chi}$ results in

$$\frac{\partial\{S_u\}}{\partial \chi} = \begin{Bmatrix} \frac{\partial u^l_i}{\partial \chi} \\ \frac{\partial u^l_{n_1}}{\partial \chi} \\ \frac{\partial u^l_{n_2}}{\partial \chi} \\ \frac{\partial u^l_{n_3}}{\partial \chi} \end{Bmatrix}; \qquad \frac{\partial\{S_v\}}{\partial \chi} = \begin{Bmatrix} \frac{\partial v^l_i}{\partial \chi} \\ \frac{\partial v^l_{n_1}}{\partial \chi} \\ \frac{\partial v^l_{n_2}}{\partial \chi} \\ \frac{\partial v^l_{n_3}}{\partial \chi} \end{Bmatrix} \tag{A37}$$

where

$$\frac{\partial}{\partial \chi}\begin{Bmatrix} u^l \\ v^l \\ w^l \end{Bmatrix} = \frac{\partial}{\partial \chi}[A_{g\to l}]\boldsymbol{V_e} + [A_{g\to l}]\frac{\partial \boldsymbol{V_e}}{\partial \chi}. \tag{A38}$$

Second, evaluating $\frac{\partial[Q]}{\partial\chi}$ results in

$$\frac{\partial[Q]}{\partial\chi} = \begin{bmatrix} 0 & 0 & 0 & 0 \\ \frac{\partial}{\partial\chi}\left(\left([\Sigma]^T[\Sigma]\right)^{-1}[\Sigma]^T\right) & \begin{matrix} -1 & 1 & 0 & 0 \\ -1 & 0 & 1 & 0 \\ -1 & 0 & 0 & 1 \end{matrix} \end{bmatrix} \tag{A39}$$

where

$$\frac{\partial}{\partial\chi}\left(\left([\Sigma]^T[\Sigma]\right)^{-1}[\Sigma]^T\right) = \frac{\partial}{\partial\chi}\left(\left([\Sigma]^T[\Sigma]\right)^{-1}\right)[\Sigma]^T + \left([\Sigma]^T[\Sigma]\right)^{-1}\frac{\partial[\Sigma]^T}{\partial\chi} \tag{A40}$$

$$\frac{\partial}{\partial\chi}\left(\left([\Sigma]^T[\Sigma]\right)^{-1}\right) = -\left([\Sigma]^T[\Sigma]\right)^{-1}\frac{\partial\left([\Sigma]^T[\Sigma]\right)}{\partial\chi}\left([\Sigma]^T[\Sigma]\right)^{-1} \tag{A41}$$

$$\frac{\partial\left([\Sigma]^T[\Sigma]\right)}{\partial\chi} = \frac{\partial[\Sigma]^T}{\partial\chi}[\Sigma] + [\Sigma]^T\frac{\partial[\Sigma]}{\partial\chi} \tag{A42}$$

References

1. Goates, J.K.; Freeman, L.B.; Hunsaker, D.F. Theory and Implementation of a Rapid Hypersonic Impact Method (HI-Mach) Part I: Aerodynamics. In Proceedings of the AIAA SciTech 2025 Forum, Orlando, FL, USA, 6–10 January 2025. [CrossRef]
2. Freeman, L.B.; Goates, J.K.; Hunsaker, D.F. Theory and Implementation of a Rapid Hypersonic Impact Method (HI-Mach) Part II: Convective Heating. In Proceedings of the AIAA SciTech 2025 Forum, Orlando, FL, USA, 6–10 January 2025. [CrossRef]
3. Freeman, L.; Goates, J.K.; Hoch, N.H.; Hunsaker, D.F.; Galbraith, M.C. Theory and Implementation of Shape Sensitivities in a Rapid Hypersonic Impact Method (HI-Mach). In Proceedings of the AIAA SCITECH 2026 Forum, Orlando, FL, USA, 12–16 January 2026; p. 0366.
4. Anderson, J.D. *Hypersonic and High Temperature Gas Dynamics*, 3rd ed.; McGraw Hill: Columbus, OH, USA, 1989.
5. Erickson, L.L. *Panel Methods—An Introduction*; NASA Technical Paper 2995; NASA: Washington, DC, USA, 1990.
6. Urraza Atue, S.; Bruce, P. Evaluation of reduced-order models for the rapid aerodynamic analysis of supersonic and hypersonic bodies. *Aeronaut. J.* **2025**, *129*, 457–484. [CrossRef]
7. Kinney, D. Aero-Thermodynamics for Conceptual Design. In Proceedings of the 42nd AIAA Aerospace Sciences Meeting and Exhibit, Reno, NV, USA, 5–8 January 2004. [CrossRef]
8. Lobbia, M.A. Rapid Supersonic/Hypersonic Aerodynamics Analysis Model for Arbitrary Geometries. *J. Spacecr. Rocket.* **2017**, *54*, 315–322. [CrossRef]
9. Gentry, A.E.; Smyth, D.N.; Oliver, W.R. *The Mark IV Supersonic-Hypersonic Arbitrary-Body Program. Volume II. Program Formulation*; Technical Report AFFDL-TR-73-159 Volume II; Air Force Flight Dynamics Laboratory: Wright-Patterson Air Force Base, OH, USA, 1973.
10. Lee, M.; Lee, J.; Kim, K.H.; Hyoungjin, K. Efficient Aerodynamic Analysis of Air-Breathing Hypersonic Vehicle using Local Surface Inclination Method based on Unstructured Meshes. *Int. J. Aeronaut. Space Sci.* **2021**, *22*, 1031–1041. [CrossRef]
11. Kline, H.; Alonso, J. Adjoint of generalized outflow-based functionals applied to hypersonic inlet design. *AIAA J.* **2017**, *55*, 3903–3915. [CrossRef]
12. Fu, J.; Qu, F.; Liu, Q.; Sun, D.; Bai, J. Multi-objective aerodynamic optimization of two-dimensional hypersonic forebody-inlet based on the heuristic algorithm. *Aerosp. Sci. Technol.* **2022**, *123*, 107470. [CrossRef]
13. Damm, K.A.; Gollan, R.J.; Jacobs, P.A.; Smart, M.K.; Lee, S.; Kim, E.; Kim, C. Discrete adjoint optimization of a hypersonic inlet. *AIAA J.* **2020**, *58*, 2621–2634. [CrossRef]
14. Kinney, D. Aerodynamic shape optimization of hypersonic vehicles. In Proceedings of the 44th AIAA Aerospace Sciences Meeting and Exhibit, Reno, NV, USA, 9–12 January 2004; p. 239.
15. Ford, B. 3 Degree-of-Freedom Aircraft Flight Analysis and Reporting (FLARE) for Trajectory Optimization. In Proceedings of the AIAA SciTech 2025 Forum, Orlando, FL, USA, 6–10 January 2025.
16. Weaver, A.S.; Hunsaker, D.F. Investigating Stability of Hypersonic Conically-Derived Waverider Vehicles. In Proceedings of the AIAA SciTech Forum, Orlando, FL, USA, 6–10 January 2025.
17. Ware, G.M. *Supersonic Aerodynamic Characteristics of a Proposed Assured Crew Return Capability (ACRC) Lifting-Body Configuration*; Technical Report NASA-TM-4136; NASA Langley Research Center: Washington, DC, USA, 1989.
18. Lees, L. Hypersonic Flow. *J. Spacecr. Rocket.* **1955**, *40*, 700–735. [CrossRef]

19. Anderson, J.D. *Modern Compressible Flow With Historical Perspective*, 3rd ed.; McGraw-Hill: Columbus, OH, USA, 2003.
20. Anderson, J.D., Jr. *Fundamentals of Aerodynamics*, 5th ed.; McGraw-Hill: Columbus, OH, USA, 2011.
21. White, F.M. *Viscous Fluid Flow*; McGraw Hill: Columbus, OH, USA, 2006.
22. Eckert, E.R.G. *Survey on Heat Transfer at High Speeds*; Technical Report ARL 189; U. S. Air Force: Wright-Patterson Air Force Base, OH, USA, 1961.
23. Meador, W.E.; Smart, M.K. Reference Enthalpy Method Developed from Solutions of the Boundary-Layer Equations. *AIAA J.* **2005**, *43*, 135–139. [CrossRef]
24. Bowcutt, K.; Anderson, J.D.; Capriotti, D. Viscous Optimized Hypersonic Waveriders. In Proceedings of the 25th AIAA Aerospace Sciences Meeting, Reno, NV, USA, 24–26 March 1987. [CrossRef]
25. Kinney, D. Aerothermal Anchoring of CBAERO Using High Fidelity CFD. In Proceedings of the 45th AIAA Aerospace Sciences Meeting and Exhibit, Reno, NV, USA, 8–11 January 2007. [CrossRef]
26. Zhao, J.; Gu, L.; Ma, H. A rapid approach to convective aeroheating prediction of hypersonic vehicles. *Sci. China Technol. Sci.* **2013**, *56*, 2010–2024. [CrossRef]
27. Kenwright, D.N. Automatic detection of open and closed separation and attachment lines. In Proceedings of the Visualization '98, Research Triangle Park, NC, USA, 18–23 October 1998; pp. 151–158. [CrossRef]
28. Kenwright, D.N.; Henze, C.; Levit, C. Feature extraction of separation and attachment lines. *IEEE Trans. Vis. Comput. Graph.* **1999**, *5*, 135–144. [CrossRef]
29. Fay, J.A.; Riddell, F.R. Theory of stagnation point heat transfer in dissociated air. *J. Aerosp. Sci.* **1958**, *25*, 73–85. [CrossRef]
30. Tauber, M.E. *A Review of High-Speed, Convective, Heat-Transfer Computation Methods*; NASA Technical Paper 2914; NASA: Washington, DC, USA, 1989.
31. Olivier, H. Influence of the velocity gradient on the stagnation point heating in hypersonic flow. *Shock Waves* **1995**, *5*, 205–216. [CrossRef]
32. Billig, F.S. Shock-wave shapes around spherical-and cylindrical-nosed bodies. *J. Spacecr. Rocket.* **1967**, *4*, 822–823. [CrossRef]
33. Dejarnette, F.R. Aerodynamic heating and surface temperatures on vehicles for computer-aided design studies. In Proceedings of the 21st Aerospace Sciences Meeting, Reno, NV, USA, 10–13 January 1983; p. 411.
34. Feller, W.V. *Investigation of Equilibrium Temperatures and Average Laminar Heat-Transfer Coefficients for the Front Half of Swept Circular Cylinders at a Mach Number of 6.9*; Technical Report; NASA: Washington, DC, USA, 1955.
35. Van Driest, E.R. *The Problem of Aerodynamic Heating*; Institute of the Aeronautical Sciences: New York, NY, USA, 1956.
36. Dannenhoffer, J. An Overview of the Engineering Sketch Pad. In Proceedings of the AIAA SCITECH 2024 Forum, Orlando, FL, USA, 8–12 January 2024; p. 1315.
37. Peter, J.E.; Dwight, R.P. Numerical sensitivity analysis for aerodynamic optimization: A survey of approaches. *Comput. Fluids* **2010**, *39*, 373–391. [CrossRef]
38. Martins, J.R.; Hwang, J.T. Review and unification of methods for computing derivatives of multidisciplinary computational models. *AIAA J.* **2013**, *51*, 2582–2599. [CrossRef]
39. Kenway, G.K.; Mader, C.A.; He, P.; Martins, J.R. Effective adjoint approaches for computational fluid dynamics. *Prog. Aerosp. Sci.* **2019**, *110*, 100542. [CrossRef]
40. Martins, J.R.; Sturdza, P.; Alonso, J.J. The complex-step derivative approximation. *ACM Trans. Math. Softw. (TOMS)* **2003**, *29*, 245–262. [CrossRef]
41. Müller, J.D.; Cusdin, P. On the performance of discrete adjoint CFD codes using automatic differentiation. *Int. J. Numer. Methods Fluids* **2005**, *47*, 939–945. [CrossRef]
42. Giles, M.B.; Pierce, N.A. An Introduction to the Adjoint Approach to Design. *Flow Turbul. Combust.* **2000**, *65*, 393–415. [CrossRef]
43. Griffin, K.P.; Fu, L.; Moin, P. Near-wall model for compressible turbulent boundary layers based on an inverse velocity transformation. *J. Fluid Mech.* **2023**, *970*, A36. [CrossRef]
44. Zhang, J.; Ji, X.; Xu, K. Treatment of wall boundary conditions in high-order compact gas-kinetic schemes. *J. Comput. Phys.* **2026**, *547*, 114541. [CrossRef]
45. Lee, S.; Yang, Y.; Kim, J.G. Evaluation of Fay and Riddell Formula under Hypersonic Flight Conditions. *Int. J. Numer. Methods Heat Fluid Flow* **2022**, *33*, 14–41. [CrossRef]
46. Eggers, A.J., Jr.; Savin, R.C.; Syvertson, C.A. The Generalized Shock-Expansion Method and Its Application to Bodies Traveling at High Supersonic Air Speeds. *J. Aeronaut. Sci.* **1955**, *22*, 231–238. [CrossRef]
47. Lee, E.; Wurster, K.E. Inviscid/boundary-layer aeroheating approach for integrated vehicle design. In Proceedings of the 55th AIAA Aerospace Sciences Meeting, Grapevine, TX, USA, 9–13 January 2017; p. 1146.
48. Cleary, J.W. *Effects of Angle of Attack and Bluntness on Laminar Heating-Rate Distributions of a 15 Deg Cone at a Mach Number of 10.6*; Technical Report; NASA: Washington, DC, USA, 1969.

49. Horvath, T.; Rhode, M.; Buck, G. Aerothermodynamic measurements on a proposed assured crew return vehicle (ACRV) lifting-body configuration at Mach 6 and 10 in air. In Proceedings of the 5th Joint Thermophysics and Heat Transfer Conference, Seattle, WA, USA, 18–20 June 1990; p. 1744.
50. Hoch, N.H. Calculation of Aerodynamic Surface Sensitivities Using the Adjoint Method in a Subsonic/Supersonic Panel Code. Master's Thesis, Utah State University, Logan, UT, USA, 2025. [CrossRef]

Disclaimer/Publisher's Note: The statements, opinions and data contained in all publications are solely those of the individual author(s) and contributor(s) and not of MDPI and/or the editor(s). MDPI and/or the editor(s) disclaim responsibility for any injury to people or property resulting from any ideas, methods, instructions or products referred to in the content.